Unlocking NIR-II Photoluminescence in 2D Copper Tetrasilicate Nanosheets Through Flame Spray Pyrolysis

Robert Nißler[1,2,3]*, Quanyu Zhou[4,5], Björn Hill[6], Sabrina L.J. Thomä[7], Lukas R.H. Gerken [1,2], Aurelio Borzi[7], Kevin Roost[1], Benjamin Mächler[1], Xosé Luís Deán-Ben[4,5], Antonia Neels[7], Sebastian Kruss[6,8], Daniel Razansky[4,5], Inge K. Herrmann[1,2,3]*

[1] Nanoparticle Systems Engineering Laboratory, Institute of Energy and Process Engineering (IEPE), Department of Mechanical and Process Engineering (D-MAVT), ETH Zurich, Sonneggstrasse 3, 8092 Zurich, Switzerland.

[2] Particles-Biology Interactions, Department of Materials Meet Life, Swiss Federal Laboratories for Materials Science and Technology (Empa), Lerchenfeldstrasse 5, 9014 St. Gallen, Switzerland.

[3] The Ingenuity Lab, University Hospital Balgrist, University of Zurich, Balgrist Campus, Forchstrasse 340, 8008 Zurich, Switzerland.

[4] Institute for Biomedical Engineering and Institute of Pharmacology and Toxicology, Faculty of Medicine, University of Zurich, Switzerland

[5] Institute for Biomedical Engineering, Department of Information Technology and Electrical Engineering, ETH Zurich, Switzerland

[6] Department of Chemistry, Bochum University, Bochum, Germany

[7] Center for X-ray Analytics, Swiss Federal Laboratories for Materials Science and Technology (Empa), Dübendorf, Switzerland

[8] Fraunhofer Institute for Microelectronic Circuits and Systems, 47057 Duisburg, Germany.

* Corresponding authors: rnissler@ethz.ch, ingeh@ethz.ch

Keywords: 2D Nanosheets, Egyptian blue, copper tetrasilicates, NIR fluorescence, NIR contrast agent

Abstract

Expanding fluorescence bioimaging into the second near-infrared spectrum (NIR-II, 1000-1700 nm) unlocks advanced possibilities for diagnostics and therapeutics, offering superior tissue penetration and resolution. Two-dimensional copper tetrasilicate (CTS) pigments (MCuSi$_4$O$_{10}$, M = Ca, Sr, Ba) are known for their brightness and stability, yet synthetic challenges have curbed their integration into bioimaging. Here, we introduce flame-spray-pyrolysis (FSP) as a versatile and scalable synthesis approach to produce ultra-bright, metastable CTS nanosheets (NS) by annealing multi-element metal oxide nanoparticles into 2D crystals. Group-II ion incorporation shifts emission into the NIR-II range, with Ba$_{0.33}$Sr$_{0.33}$Ca$_{0.33}$CuSi$_4$O$_{10}$ peaking at 1007 nm, while minor Mg-doping induces a hypsochromic shift and extends fluorescence lifetimes. The engineered CTS achieve quantum yields up to 34%, supporting NS high-frame-rate imaging (>200 fps). These unique properties enable CTS-NS to serve as powerful contrast agents for super-resolution NIR bioimaging, demonstrated in vivo through transcranial microcirculation mapping and macrophage tracking in mice using diffuse optical localization imaging (DOLI). This pioneering synthesis strategy unlocks wavelength-tunable NS for advanced NIR-II bioimaging applications.

Introduction

Pushing the boundaries of fluorescence bioimaging into the second near-infrared spectrum (NIR-II, 1000-1700 nm) is pivotal for enhancing its diagnostic and therapeutic capabilities in biomedical research. This spectrum holds immense potential for deep-tissue imaging due to reduced autofluorescence and light scattering.[1,2] While conventional agents have demonstrated efficacy in the first near-infrared (NIR-I, 700-950 nm) spectral window, they often perform inadequately in the NIR-II spectrum, underscoring the need for novel contrast agents designed specifically for this range. Current fluorophores used in this bio-transparency window include organic dyes, such as indocyanine green (ICG),[3] as well as inorganic structures like quantum dots (QD),[4–6] single-walled carbon nanotubes (SWCNTs),[7] and rare-earth element-doped nanoparticles.[8] Each aforementioned material offers distinct benefits, yet the ideal material would be characterized by photostability, a significant Stokes shift, and a high photoluminescence quantum yield (PL-QY) within the NIR-II window. Additionally, the ideal material should ensure biocompatibility, possess advantageous colloidal properties, and be amenable for surface functionalization. Such attributes would greatly enhance the imaging performance of existing bioimaging tools by improving spatial resolution and penetration depth, paving the way for functional and molecular imaging. This, in turn, would expand the applicability of optical bioimaging in disease diagnostics, treatment evaluations, and image-guided surgeries.[9]

A particular class of nanostructured pigments, renowned for centuries but recently experiencing a resurgence in interest, are two-dimensional (2D) copper tetrasilicates (CTS) with the general structure MCuSi$_4$O$_{10}$, where M denotes for the alkaline earth metals Ca, Sr, or Ba.[10–12] The most renowned inosilicate among these is CaCuSi$_4$O$_{10}$, commonly referred to as Egyptian blue. Its synthesis traces back to Ancient Egypt (circa 2500 BC), cementing its status as the earliest known pigment crafted by humanity. Its structural counterpart, BaCuSi$_4$O$_{10}$ (known as Han Blue), emerged in ancient Chinese pottery during the Han dynasties (circa 220 BC – 220 AD).[13] Intriguingly, the vivid hues of these materials have withstood the toll of time, retaining their unique luminescent attributes, particularly a potent fluorescence emission in the NIR-I at about 910 nm.[2,14,15] CTSs embodying a multitude of the aforementioned desired characteristics, emerge as promising candidates for bioimaging and sensing applications.[16] Yet their full potential, particularly as NIR-II emissive agents, remains relatively unexplored but holds immense promise. These blue pigments can be synthesized by various approaches,[16] creating bulk material with different levels of purities and crystal sizes. Most commonly, salt-flux or solid-state synthesis is used, based on e.g. the ancient process whereas respective minerals are finely grinded and heated to 900 °C over several hours, while sintering to the desired crystal phase takes place at the grain boundaries.[13] Additionally, methods like hydrothermal synthesis can produce mesoporous microspheres of narrow size distribution, however without the possibility for straightforward compositional engineering and being limited in production scale.[17] Previous studies have unveiled that the laminar architecture of the CTSs can be exfoliated into 2D nanosheets (NS) as thin as a single crystal lattice.[10,12] Remarkably, these NS resist photobleaching and exhibit a polarization-neutral emission, setting them apart as an promising NIR reference material for sensing applications.[18,19] To obtain NS, multiple approaches are known, combining breaking down the crystal structure and exfoliating it via ball milling, sonication, prolonged stirring in solvents or a combination from all of them.[16,20,21] However, in recent studies it became apparent that intensified mechanical stress due to exfoliating and milling these materials down to the nanoscale substantially degraded their fluorescence emission properties.[22] These findings significantly constrain potential applications and underscore the necessity for a scalable and tunable synthesis route that can produce highly fluorescent nanomaterials for use as high-performance bioimaging agents.

In this work, we report the synthesis of NIR-II emissive CTS-NS, offering new possibilities for bioimaging techniques. To enable the NIR-II emission of CTSs, we demonstrate that bottom-up NS synthesis can be accomplished by annealing multi-doped nanoparticles, initially created through flame-spray synthesis, into 2D nanocrystals. Stoichiometric metal-organic precursor solutions are injected into a CH$_4$/O$_2$ flame, where controlled combustion of the organic solvent and subsequent nucleation of metal oxides form nanoparticles with a homogeneous elemental distribution. Annealing these FSP-derived particles enables the controlled

2

incorporation of group-II cations into the CTS crystal structure, yielding NIR-emissive engineered materials that can be exfoliated into 2D-NS. These NS are then harnessed to assess their potential for real-time, deep-tissue, super-resolution bioimaging, enabling the mapping of the transcranial cortical microcirculation in mice using diffuse optical localization imaging (DOLI) and tracking individual macrophages across cerebral regions.

Results

Flame-spray pyrolysis-based synthesis of group-II cation-doped copper silicates

Historical synthesis approaches rely on the mixing and sintering of mineral phases containing elements, leading to phase defects at the grain boundaries. To address this limitation, we employ a highly robust and industrially viable method known as flame-spray-pyrolysis (FSP) to obtain metal-oxide particles.[23] In this process, metal organic precursors with the desired elemental ratio are dissolved in organic solvents and injected into a CH_4/O_2 flame. Temperatures within the flame can reach >3300 K whereas the spray exhibits velocities of about 150 m/s, causing the organic solvent to combust and leading the metal atoms to nucleate and form respective oxides.[24,25] The emerging nanoparticles are then collected on an above-mounted filter (Figure 1a). However, these FSP-born silicate particles are initially amorphous and about 30 nm in size, as observed via TEM analysis (Figure 1b*i*), and exhibit a homogeneous distribution of the precursor elements Cu, Si, O, and *M*, where *M* = Ca, Sr, or Ba. Annealing the nanoparticles at a specific temperature (Figure 1b*ii*) results in bulk CTS powder with the desired 2D crystal structure, which can be further exfoliated to the single/few atomic layer NS regime (Figure 1b*iii*).
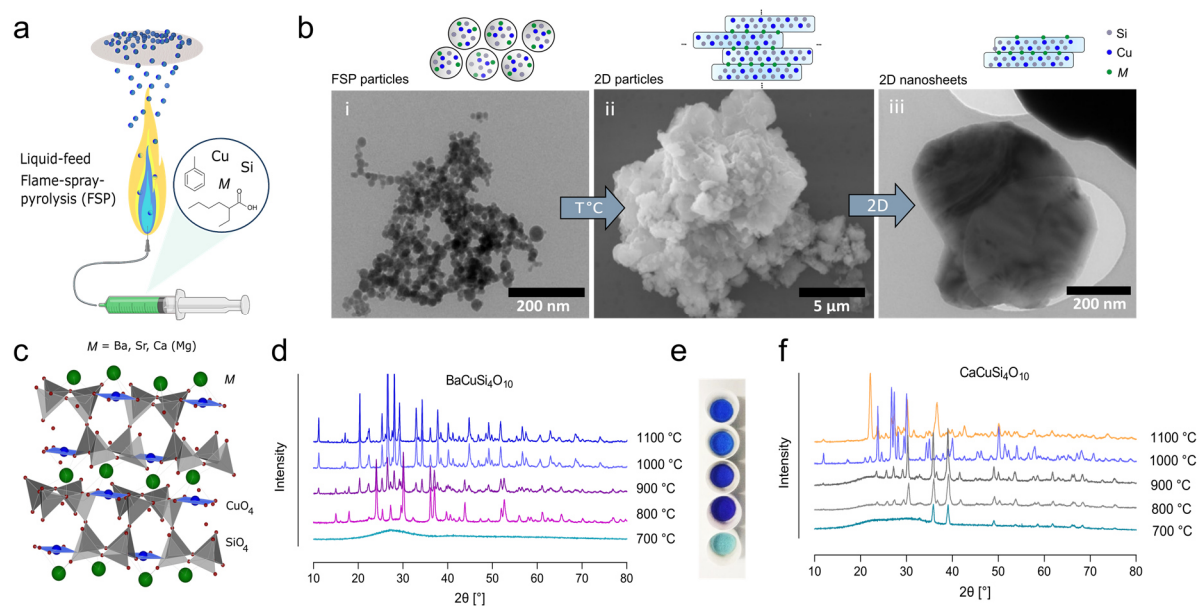

Figure 1: Flame-spray-pyrolysis of 2D copper tetrasilicates *M*CuSi₄O₁₀. a) Schematic representation of the synthesis process. Metal-organic precursor solution in toluene and 2-EHA is fed into a CH_4/O_2 flame, whereas emerging NP are collected on an above-mounted filter. This synthesis procedure allows compositional engineering of the emerging nanosheets (NS). b) Electron microscopic visualization of the NS synthesis with a schematic representation. i - TEM image of the ~30 nm large, spherical as-prepared FSP NPs with homogeneous elemental distribution. ii – Annealing of the FSP particles leads to the formation of 2D materials with the desired crystal lattice (SEM image). iii –2D material can be dispersed and exfoliated down to the nanosheet regime (TEM image). c) Visualization of the tetragonal phase (*P4/n c c*; #130) of *M*CuSi₄O₁₀. Alkaline earth metals (*M*) link monolayers of silica-tetrahedra with square planar coordinated copper ions. d) XRD patterns of NPs with the nominal chemical composition of BaCuSi₄O₁₀, sintered at different temperatures. Picture of veils containing these NP in (e). Annealing of as-prepared FPS particles at 1000 °C or 1100 °C for 10 min leads to the near pure formation of the desired tetragonal crystal phase. f) XRD pattern of annealed NPs forming CaCuSi₄O₁₀ at 1000 °C. The colors of each XRD profile visualize the appearance of the nano-powder. Likewise, FSP-synthesis can also be used to produce SrCuSi₄O₁₀ (Supplementary Figure S2).

During this process, the crystal phase can be precisely tuned through screening of different annealing temperatures, facilitated by thermogravimetric analysis (TGA), until the tetragonal *P 4/n c c* space group is observed via X-ray diffraction (XRD) analysis (Figure 1c). For example, as seen in the Ba-containing CTS variation (Figure 1d, e), the powder with primary FSP particles changes color from green-cyan (FSP material) to purple (800°C) to dark blue (1000-1100°C), consistent with corresponding XRD analysis identifying the formation of tetragonal *I4₁ /acd* space group at 800°C, followed by a miscellaneous phase at 900°C, and finally the desired *P 4/n c c* phase at 1000-1100°C. To obtain other MCuSi$_4$O$_{10}$ variations, only the exchange of the respective alkaline earth metal solution during preparation of the FSP precursor solution is needed. Annealing similar nanoparticles with M = Ca results in the formation of CaCuSi$_4$O$_{10}$ (Cuprorivaite, Egyptian blue) at 1000°C (Figure 1f) within just a few minutes (Supplementary Figure S1), while the bulk material exhibits a light blue color. This modular synthesis approach is therefore capable of yielding all known CTS materials, including SrCuSi$_4$O$_{10}$ (Strontium Blue), solely by modifying the elemental composition and ratio via the FSP process (Supplementary Figure S2).

The surface area of the nanoparticles was found to decrease during the annealing process from about 95-120 g/m^2 of the FSP material to 3-13 g/m^2 of the CTS phase, as measured by Brunauer-Emmett-Teller (BET) analysis (Supplementary Table T1). Rietveld refinement confirms that NS variations are yielded with high purity, containing >98% of the desired crystal phase (Supplementary Figure S3). It should be noted that attempts to directly synthesize copper tetrasilicate material using the FSP process were unsuccessful, even after encasing the flame aperture with a glass mantle to increase temperature and prolong circulation time above the flame.

Synthesis of assorted bi-doped group-II cation copper tetrasilicates

Further leveraging the modular and universal FSP synthesis approach, we then synthesized mixed alkaline earth metal CTS. By solely exchanging the respective fraction of alkaline earth metal precursor solution, an equimolar mixture of Ca and Sr led to the synthesis of Sr$_{0.5}$Ca$_{0.5}$CuSi$_4$O$_{10}$ (Figure 2a, Supplementary Figure S4). The XRD reflexes (Figure 2b) of the mixed phase lays in between both single phases resulting in shifted *P 4/n c c* lattice parameters of $a = 7.33$ Å and $c = 15.39$ Å.
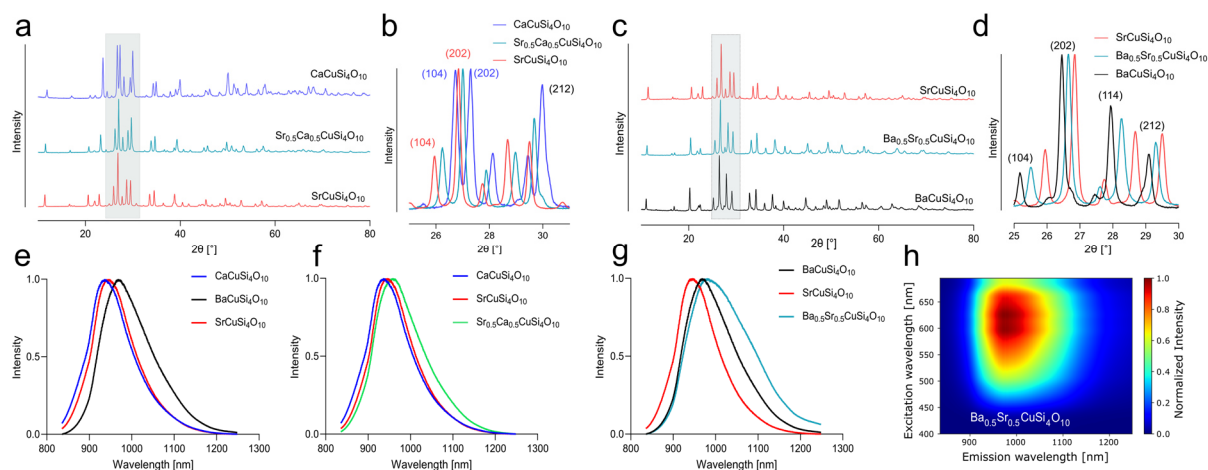

Figure 2: FSP-based syntheses of mixed Ba-Sr and Sr-Ca copper tetrasilicates. a) XRD pattern of SrCuSi$_4$O$_{10}$ and CaCuSi$_4$O$_{10}$ and its mixed form Sr$_{0.5}$Ca$_{0.5}$CuSi$_4$O$_{10}$ with zoom in b) into the region between 25-31 °2θ highlighting the shifted (202) reflex of the mixed material. c) XRD pattern of BaCuSi$_4$O$_{10}$ and SrCuSi$_4$O$_{10}$ and its stoichiometrically exchanged form Ba$_{0.5}$Sr$_{0.5}$CuSi$_4$O$_{10}$ with zoom in d) into the region between 25-30 °2θ highlighting the similarly shifted reflexes. e) PL emission spectra of FSP-synthesized mono-alkaline earth metal CTS. f) PL emission spectra of Sr$_{0.5}$Ca$_{0.5}$CuSi$_4$O$_{10}$. g) PL emission spectra of Ba$_{0.5}$Sr$_{0.5}$CuSi$_4$O$_{10}$. h) 2D excitation-emission PL map for Ba$_{0.5}$Sr$_{0.5}$CuSi$_4$O$_{10}$.

Analogous experiments with equimolar combination of Ba and Sr precursors lead to the formation of $Ba_{0.5}Sr_{0.5}CuSi_4O_{10}$ as depicted in Figure 2c. Again, the incorporation of smaller ions (Sr) into the $BaCuSi_4O_{10}$ crystal lattice resulted in a shift of the XRD reflexes towards greater 2θ values (Figure 2d). The lattice parameters of the $Ba_{0.5}Sr_{0.5}CuSi_4O_{10}$ phase are of $a = 7.39$ Å and $c = 15.89$ Å. Rietveld refinement furthermore confirmed the synthesis of high purity doped NS material (Supplementary Figure S5). NIR-fluorescence spectroscopic characterization of the resulting material revealed the characteristic emission profile of the CTS with $MCuSi_4O_{10}$ with M = Ca, Ba, Sr (Figure 2e). Comparing their emission to the Sr-Ca intermixed CTS material (Figure 2f), shows a slightly red-shifted emission for the formed $Sr_{0.5}Ca_{0.5}CuSi_4O_{10}$ with $\lambda_{max} = 957$ nm. The equimolar combination of Ba-Sr, however, showed a significant bathochromic shift with $\lambda_{max} = 981$ nm (Figure 2g), accompanied by a general broadening of the NIR-emission of $Ba_{0.5}Sr_{0.5}CuSi_4O_{10}$, as seen in the 2D excitation-emission PL map in Figure 2h. The PL emission maxima, as well as the UV-Vis-NIR absorbance spectra (Supplementary Figure S6) of the known CTS are in accordance with previous reports.[16] The spectral red-shift of $Sr_{0.5}Ca_{0.5}CuSi_4O_{10}$ is in agreement with a recent report, identifying an equimolar ratio of Sr to Ca (1:1) as most optimal ratio to achieve an enhanced bathochromic emission shift.[26] To our knowledge, ours is the first report of the significantly bathochromic-shifted emission properties of $Ba_{0.5}Sr_{0.5}CuSi_4O_{10}$. The UV-Vis-NIR absorbance spectra of both bi-doped group-II cation CTS showed a slight broadening of the B_{1g}-E_g transition, as well as a minor hyperchromic shift in A_{1g}-E_g transition (Supplementary Figure S7).

FSP-Synthesis gives access to meta-stable Ba-Ca copper tetrasilicates

Given that the synthesis of $Sr_{0.5}Ca_{0.5}CuSi_4O_{10}$ and $Ba_{0.5}Sr_{0.5}CuSi_4O_{10}$ is reported,[26–31] albeit using poorly scalable methods, we aimed to evaluate whether the FSP synthesis approach could yield alkaline earth metal combinations explicitly described as "forbidden" or inaccessible through established methods, such as the combination of Ba and Ca cations within the CTS lattice.[13,31] We hypothesized that the optimal elemental distribution within the FSP-derived primary particles could facilitate a homogeneous alkaline earth metal distribution within the annealed CTS-NSs.

The combination of such mixed forms could be tested straightforwardly by altering the Ba and Ca precursor ratios, whereby the XRD pattern of the resulting materials are presented in Figure 3a given as the synthesis ratio of the alkaline earth metals (M_S). Up to an M_S = $Ba_{0.75}Ca_{0.25}$ and M_S = $Ba_{0.5}Ca_{0.5}$ a predominant, non-shifted $BaCuSi_4O_{10}$ phase was observed, with a minor reflex of a shifted, Ba-Ca mixed CTS phase as highlighted in Figure 3a and 3b. We correlate the formation of such a $Ba_xCa_{1-x}CuSi_4O_{10}$-phase with a significantly impacted PL emission, as samples exhibited a bathochromic emission shift, highlighted for M_S = $Ba_{0.5}Ca_{0.5}$ in Figure 3c. However, this shifted emission features, as measure for a successful $Ba_xCa_{1-x}CuSi_4O_{10}$-phase formation seemed to be annealing temperature dependent. M_S = $Ba_{0.5}Ca_{0.5}$ annealed at 900°C exhibited an emission maximum of 984 nm with an emission tail spanning far into the NIR-II spectral window (Figure 3d, Supplementary Figure S8), containing about 60% of a Ba-Ca mixed CTS phase as evaluated by Rietveld refinement (Supplementary Figure S9). Annealing at 1000°C or 1100°C showed only a slight emission shift compared to $BaCuSi_4O_{10}$, containing only about 31% of $Ba_xCa_{1-x}CuSi_4O_{10}$ (Supplementary Figure S9). Most interestingly, a synthesis ratio of M_S = $Ba_{0.15}Ca_{0.85}$ and M_S = $Ba_{0.25}Ca_{0.75}$ resulted in the near exclusive formation of a Ba-Ca mixed copper tetrasilicate phase, possessing intermediate lattice parameters (Figure 3e). Rietveld refinement revealed that M_S = $Ba_{0.15}Ca_{0.85}$ annealed for 10 min at 1000°C contains 87% of a $Ba_xCa_{1-x}CuSi_4O_{10}$ phase with lattice parameters of $a = 7.31$ Å and $c = 15.18$ Å. M_S = $Ba_{0.25}Ca_{0.75}$ annealed for 10 min at 1000°C contained 93% of a $Ba_xCa_{1-x}CuSi_4O_{10}$ phase with lattice parameters of $a = 7.32$ Å and $c = 15.38$ Å. However, both samples surprisingly contained a second inter-mixed Ba-Ca phase, representing 13% and respectively 7% of the material with

5

significantly larger lattice parameters (Supplementary Figure S11). Based on these lattice parameters, it is expected that the observed Ba-Ca mixed CTS phases vary in their Ba-Ca ratios. However, the exact compositions could not be determined through Rietveld refinement due to significant overlap in the reflections of the two different tetragonal *P 4/n c c* phases, particularly in the 25–32° 2Θ region. Analyzing the PL emissions of the materials revealed a strong bathochromic shift for $M_S = $ Ba$_{0.25}$Ca$_{0.75}$ with an $\lambda_{max} = 993$ nm and a significant broadening towards the NIR-II (Figure 3f; Supplementary Figure S12). $M_S = $ Ba$_{0.15}$Ca$_{0.85}$ on the other hand, showed a drastic shift with $\lambda_{max} = 963$ nm compared to CaCuSi$_4$O$_{10}$ ($\lambda_{max} = 936$ nm) indicating, that exchanging 15% of the alkaline earth metals with Ba only slightly alters the crystal lattice but strongly impacts the fluorescence emission. The obtained Ba-Ca intermixed phase, however, seemed to be meta-stable, as extended annealing times of 2-24h lead to an enhanced segregation into minorly doped Ba- and Ca-phases (Supplementary Figure S13 and S10), accompanied by a decreased bathochromic shift (Figure 3g). To further verify the creation of a single Ba$_x$Ca$_{1-x}$CuSi$_4$O$_{10}$-phase on a nanoscale level, we performed scanning transmission electron microscopy (STEM) analysis of single $M_S = $ Ba$_{0.25}$Ca$_{0.75}$ NS. The resulting HAADF image and corresponding electron diffraction (ED) pattern are shown in Figure 3h, suggesting a highly crystalline material with a typical ED pattern for materials of the *P 4/n c c* space group.
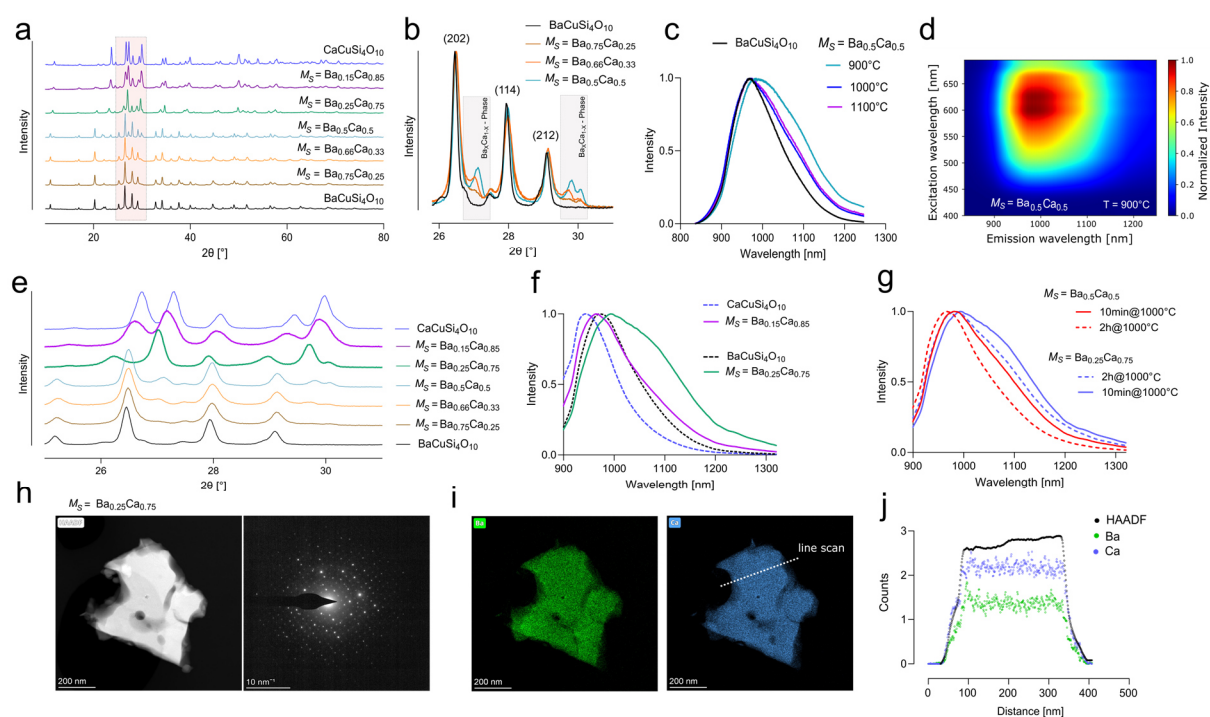

Figure 3: FSP-based syntheses enable intermixed Ba-Ca copper tetrasilicates. a) XRD pattern of BaCuSi$_4$O$_{10}$ and CaCuSi$_4$O$_{10}$ and their mixed forms, expressed as the synthesis ratio of the alkaline earth metals (M_S) with zoom in b) visualizing the co-existence of the BaCuSi$_4$O$_{10}$-phase and a intermixed Ba$_x$Ca$_{1-x}$CuSi$_4$O$_{10}$-phase until $M_S = $ Ba$_{0.5}$Ca$_{0.5}$. c) PL emission spectra of $M_S = $ Ba$_{0.5}$Ca$_{0.5}$ annealed at different temperatures. d) 2D excitation-emission PL map for $M_S = $ Ba$_{0.5}$Ca$_{0.5}$ annealed at 900°C, as it contains about 60% Ba$_x$Ca$_{1-x}$CuSi$_4$O$_{10}$evaluated by Rietveld refinement. e) XRD pattern of between BaCuSi$_4$O$_{10}$ and CaCuSi$_4$O$_{10}$ and their mixed forms, between 25-31° 2θ highlighting the existence of shifted, single phases at $M_S = $ Ba$_{0.15}$Ca$_{0.85}$ and $M_S = $ Ba$_{0.25}$Ca$_{0.75}$. f) PL emission spectra of CTSs, originated from various Ba-Ca synthesis ratios. g) Influence of annealing time on the PL emission spectra of $M_S = $ Ba$_{0.5}$Ca$_{0.5}$ and $M_S = $ Ba$_{0.25}$Ca$_{0.75}$ indicating the existence of a meta-stable Ba$_x$Ca$_{1-x}$CuSi$_4$O$_{10}$-phase, exhibiting a bathochromic shift in the emission maxima. h) STEM analysis of a single $M_S = $ Ba$_{0.25}$Ca$_{0.75}$ NS shown as HAADF image and corresponding electron diffraction (ED) pattern. i) EDX-based elemental mapping of Ba and Ca. j) Line-profile (50-pixel width) showing a homogeneous distribution of Ba and Ca within the NS.

Further EDX-based elemental mapping showed a strong co-localization between Ba and Ca (Figure 3i; full elemental mapping in Supplementary Figure S14) whereas a line profile horizontally to the NS revealed a homogeneous distribution of both alkaline earth metals within the NS (Figure 3j). Moreover, EDX analysis yielded the alkaline earth metals ratio (M_{EDX}) between Ba and Ca of $M_{EDX} = Ba_{0.78}Ca_{0.22}$, overall, very close to the FSP-based precursor ratio. To our knowledge, this is the first time intermixed Ba-Ca copper tetrasilicates were synthesized. Likely due to the differences in atomic size with Ba = 2.24 Å and Ca = 1.97 Å, the incorporation is unfavored and allows no continuous mixing under all tested synthesis ratios (M_S). As a consequence, in excess Ba-conditions ($M_S = Ba_{0.75}Ca_{0.25}$) a predominant $BaCuSi_4O_{10}$ phase will form with shifted emission features, but no significant shift in XRD pattern, whereas under excess Ca-conditions ($M_S = Ba_{0.25}Ca_{0.75}$) nearly a single, intermixed phase is observed with significantly shifted emission properties and XRD reflexes. However, as the PL of $M_S = Ba_{0.75}Ca_{0.25}$ shows a red-shifted emission maxima and a broadening towards the NIR-II (see Supplementary Figure S12), but only a marginal $Ba_xCa_{1-x}CuSi_4O_{10}$-phase according to the XRD pattern, we attribute the shifted emission to a slight doping of the main $BaCuSi_4O_{10}$ phase, without significantly altering the XRD reflex positions. This implies that the photoluminescence behavior of the NS might be more sensitive to doping with other alkaline earth metals compared to the occurrence of an overall shift in the crystal phase and XRD pattern, as doping levels might differ to induce significant changes in both analytical measurements. As a consequence thereof, we introduce the nomenclature of doped CTS composites in order of heavier to lighter alkaline earth metals, in cases where an altered crystal phase could be confirmed by XRD. Other synthesis ratios (M_S) that resulted in insignificant shifts in XRD but caused significant modulation of the PL emission properties, compared to the native phase, are referred to as M-doped CTS. Previous studies already indicated that e.g. minor doping of $CaCuSi_4O_{10}$ could induce a shift in emission spectra, however without significant altering of

lattice parameters.[32] This leads us to the conclusion that at higher Ba-Ca ratios, a Ca-doped $BaCuSi_4O_{10}$ phase is generated, whereas equimolar rations of Ba-Ca leads to the co-existence of a likely Ca-doped $BaCuSi_4O_{10}$ phase and a mixed $Ba_xCa_{1-x}CuSi_4O_{10}$ phase. Finally, under excess Ca to Ba conditions, a near exclusive intermixed $Ba_xCa_{1-x}CuSi_4O_{10}$ phase is detected. In contrast to the mixed phases of $Sr_{0.5}Ca_{0.5}CuSi_4O_{10}$ and $Ba_{0.5}Sr_{0.5}CuSi_4O_{10}$, the Ba-Ca phases such as $Ba_{0.25}Ca_{0.75}CuSi_4O_{10}$ was found to be meta-stable, as prolonged annealing times would lead to the segregation of the mixed phases. This implies that the intermixed Ba-Ca sample could not reach its equilibrium, shining light on the synthesis process of the doped CTS-NS. As starting from homogenously distributed elements within the FSP-derived particles, the thermal-induced rearrangement to the 2D crystal lattice seems to occur faster than the segregation into stable, mono-alkaline earth metal CTS.

Multielement doping of copper tetrasilicates tailors the PL emission

Building up on the successful combination of Ba-Ca, we investigated the multi-element-doping of NS and the synthesis with equimolar ratios of Ba, Sr and Ca precursors, which showed again homogeneous distribution within the FSP-particles (Supplementary Figure S15). Annealing at 1000°C suggests the formation of $Ba_{0.33}Sr_{0.33}Ca_{0.33}CuSi_4O_{10}$. The corresponding XRD pattern depicted in Figures 4a and 4b reveals a slight shift in the peak positions of the doped tetragonal *P4/n c c* phase, along with substantial peak broadening. Notably, Rietveld refinement alone could not quantify the composition of the multielement-doped material, as all three cations occupy the same position. Similar agreement values would be obtained even when the refinement was performed with only Ba and Sr sharing this position. The fluorescence emission of the resulting nanomaterial shows a broadened, bathochromic shift, compared to $Ba_{0.5}Sr_{0.5}CuSi_4O_{10}$ (Figure 4c), with λ_{max} = 1007 nm and Full Width at Half Maximum (FWHM) of 197 nm. This broad emission spans far into the NIR-II spectral window, as seen in the 2D excitation-emission PL map in Figure 4d. The

$Ba_{0.33}Sr_{0.33}Ca_{0.33}CuSi_4O_{10}$ material was found not to undergo significant changes with prolonged annealing times (Supplementary Figure S16), indicating a stable formation of multi-element doped NS. Complementary STEM analysis on a single $Ba_{0.33}Sr_{0.33}Ca_{0.33}CuSi_4O_{10}$ NS was performed to access the structure and elemental distribution with nanoscale resolution. Figure 4e shows the HAADF image and corresponding electron diffraction pattern of the NS, accentuating the highly crystalline nature of the doped material with a typical ED pattern for the respective CTS material class. EDX-based elemental mapping indicates a strong co-localization between Ba, Sr and Ca (Figure 4f), whereas the corresponding line scan in Figure 4g indicates a near homogeneous distribution of the three alkaline earth metals. However, analysis of multiple $Ba_{0.33}Sr_{0.33}Ca_{0.33}CuSi_4O_{10}$ NSs indicated a general trend of homogeneous distribution of Sr within the NS lattice, whereas the local concentration of Ba and Ca reciprocally could slightly vary, however without segregating into separate phases (Supplementary Figure S17). $Ba_{0.33}Sr_{0.33}Ca_{0.33}CuSi_4O_{10}$ annealed for 24h at 1000°C exhibited a minor Ca-containing phase, resulting in a slight underrepresentation of Ca in the overall EDX analysis of the doped NS. The alkaline earth metals ratio quantified by EDX was $M_{EDX} = Ba_{0.36}Sr_{0.39}Ca_{0.25}$, closely matching the FSP-based precursor ratio. To complete our efforts to dope the copper tetrasilicates with group-II cations, we aimed for the introduction of Mg into the NS crystal lattice.
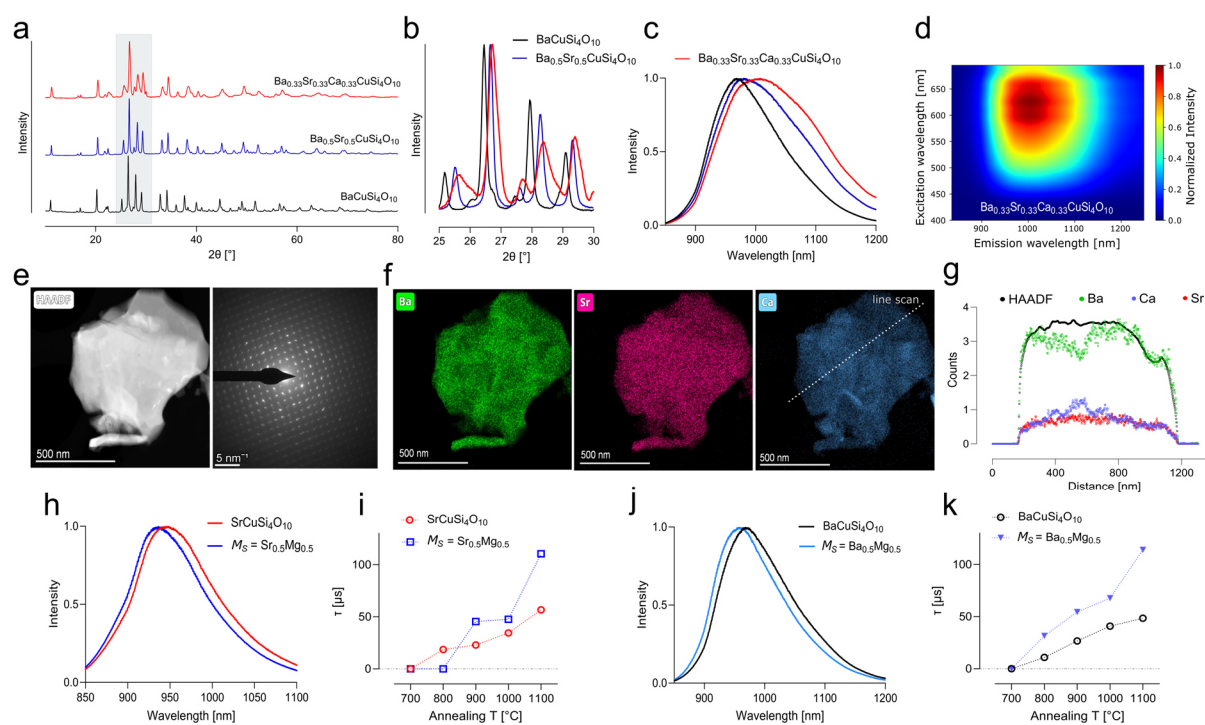

Figure 4: Multielement doping of copper tetrasilicates. a) XRD pattern of $BaCuSi_4O_{10}$ compared to the multi-element doped version $Ba_{0.33}Sr_{0.33}Ca_{0.33}CuSi_4O_{10}$ with zoom in b) into the region between 25-30° 2θ visualizing the shifted and broadened reflexes. c) PL emission spectra of $Ba_{0.33}Sr_{0.33}Ca_{0.33}CuSi_4O_{10}$ shows a significant bathochromic shift compared to $Ba_{0.5}Sr_{0.5}CuSi_4O_{10}$. d) 2D excitation-emission PL map of $Ba_{0.33}Sr_{0.33}Ca_{0.33}CuSi_4O_{10}$. e) STEM analysis of a single $Ba_{0.33}Sr_{0.33}Ca_{0.33}CuSi_4O_{10}$ NS shown as HAADF image and corresponding electron diffraction (ED) pattern. f) EDX-based elemental mapping of Ba, Sr and Ca. g) Line-profile (50-pixel width) showing a near homogeneous distribution of Ba, Sr and Ca within the NS. h) PL emission spectra of Mg-doped-$SrCuSi_4O_{10}$, showing a blue-shifted emission compared to the non-Mg-doped material. i) Fluorescence lifetimes of CTSs presented in (k) showing increased lifetime values for Mg-doped- $SrCuSi_4O_{10}$ (mean ± SD). j) PL emission spectra of the Mg-doped-$BaCuSi_4O_{10}$, resulting from $M_S = Ba_{0.5}Mg_{0.5}$ showing a blue-shifted emission maxima compared to bare $BaCuSi_4O_{10}$. k) Fluorescence lifetime modulation through annealing temperature variation indicating enhanced lifetimes for Mg-doped-$BaCuSi_4O_{10}$ (mean ± SD).

Again, solely by exchanging equimolar ratios of the respective alkaline earth metal from the FSP precursors solution, amorphous FSP-NPs were generated that obtain a homogeneous distribution of all admixed elements (Supplementary Figure S18). Annealing of M_S = $Sr_{0.5}Mg_{0.5}$ particles formed CTS material, processing a light blue color, however, further XRD analysis could not identify significant shifts of the $P4/n\ c\ c$ phase towards larger reflex positions, as they would be expected for incorporation of smaller Mg atoms (1.6 Å) into the crystal lattice (Supplementary Figure S19).

In contrast, fluorescence spectroscopic analysis revealed 12 nm blue-shifted emission maxima for M_S = $Sr_{0.5}Mg_{0.5}$ with λ_{max} = 935 nm, compared to the non-doped emission of $SrCuSi_4O_{10}$ (λ_{max} = 947 nm). Simultaneously, the obtained NS material exhibited increased fluorescence lifetime, reaching a maximum when annealed at 1100°C for 10 min of τ = 110 µs (Figure 4i) and of τ = 153 µs, when annealed for 3h. Similar trends were observed for M_S = $Ba_{0.5}Mg_{0.5}$ NS, possessing 10 nm blue-shifted emission maxima of λ_{max} = 958 nm compared to $BaCuSi_4O_{10}$ (Figure 4j). The fluorescence lifetime of the obtained NS increased to τ = 114 µs, when annealed at 1100°C for 10min (Figure 4k) and to τ = 128 µs after annealing at 1000°C for 24h (Supplementary Figure S19). Complementary STEM analysis showed a strong segregation of the Mg-containing phases, however with traces of Mg (<0.5% atomic fraction) within the non-segregated CTSs. These findings led us to the conclusion, that the incorporation of Mg into the crystal phase is highly unfavored and happens only in minor quantities, which does not significantly impact the overall lattice parameters as evaluated by Rietveld refinement (Supplementary Figure S20 and S21). However, we attribute the altered photoluminescence properties of the materials, such as blue-shifted emission and increased lifetimes, to an overall slight Mg-doping of the copper tetrasilicates based on EDX. Further particles were synthesized with M_S = $Ca_{0.9}Mg_{0.1}$, M_S = $Sr_{0.33}Ca_{0.33}Mg_{0.33}$, M_S = $Ba_{0.33}Sr_{0.33}Mg_{0.33}$ and M_S = $Ba_{0.25}Sr_{0.25}Ca_{0.25}Mg_{0.25}$. The annealed materials did not show major shifts for the XRD

analysis, only for M_S = $Ba_{0.33}Sr_{0.33}Mg_{0.33}$ and M_S = $Ba_{0.25}Sr_{0.25}Ca_{0.25}Mg_{0.25}$ the $P4/n\ c\ c$ lattice parameter c was found slightly shifted towards smaller values (Supplementary Figure S22). All annealed materials, however, obtained a minorly blue-shifted emission maxima, compared to the non-Mg-doped counterpart, whereas for M_S = $Sr_{0.33}Ca_{0.33}Mg_{0.33}$ also significantly larger fluorescence lifetimes were detected (Supplementary Figure S23). STEM analysis found again strong segregation of the Mg-containing phases, as well as a traces of Mg (<0.5% atomic fraction) within the non-segregated copper tetrasilicates NSs (Supplementary Figure S24-S26). For M_S = $Ca_{0.9}Mg_{0.1}$, different trends during annealing were observed, reaching its maxima during 10 min-sintering at 1100°C (Supplementary Figure S27). Overall, we attribute the shifted fluorescence properties of the described materials to slight Mg-introduction, yielding Mg-doped-$CaCuSi_4O_{10}$ Mg-doped-$Ba_{0.5}Sr_{0.5}CuSi_4O_{10}$, Mg-doped-$Sr_{0.5}Ca_{0.5}CuSi_4O_{10}$ and Mg-doped-$Ba_{0.33}Sr_{0.33}Ca_{0.33}CuSi_4O_{10}$. However, as the emission maxima is known to depend on the exact group-II cation ratio,[26] the introduction and segregation of Mg could possibly change this aspects in multielement doping of CTSs. Since similar trends of fluorescence modulation were found in Mg-doped-$SrCuSi_4O_{10}$ and Mg-doped-$BaCuSi_4O_{10}$, we attribute the observed changes to an overall minor Mg-doping, rather than a modulated alkaline earth metal ratio.

Engineering of copper tetrasilicates shifts emission to NIR-II window

After synthesizing this full set of NS combinations, including novel mixed phases of Ba-Ca and Ba-Sr-Ca CTS, their potential for biomedical imaging was assessed. An optimal bioimaging probe would meet two major requirements: a red-shifted fluorescence emission in the NIR-II spectral window as imaging modalities improve due to decreased scattering and tissue absorption[1,2] and a bright emittance, characterized by a high PL-QY. Besides the previously mentioned bathochromic shift in emission maxima of the multielement-doped NS, a general broadening of the emission including a

tail reaching far into the NIR-II was detected (Figure 5a). To quantify the proportion of NIR emission, we subdivided the spectra into two parts, whereas the NIR-I included the emission up to 1000 nm and the NIR-II does include all emission above. As seen from Figure 5b, about 25% of the emission of $SrCuSi_4O_{10}$ spans within the NIR-II, whereas for $BaCuSi_4O_{10}$ it is 37%. For $Ba_{0.5}Sr_{0.5}CuSi_4O_{10}$ already the majority (58%) of the emitted photons are detected within the NIR-II, whereas a maximum was observed for $Ba_{0.33}Sr_{0.33}Ca_{0.33}CuSi_4O_{10}$ with 67% and $Ba_{0.25}Ca_{0.75}CuSi_4O_{10}$ with 68%. Those observed emission properties translate into altered energy

levels for the Cu^{2+} ion, located in the tetragonally distorted crystal field environment, shown as simplified energy diagram in Figure 5c. For all CTSs with the common structure of $MCuSi_4O_{10}$, the Cu^{2+} is in square-planar coordination with four oxygen atoms forming a near perfect D_{4h} symmetry due to the Jahn–Teller effect and lattice constraints, whereas in an octahedral ligand field (O_h symmetry), the ^2D ground state of free Cu^{2+} ions split into T_{2g} and E_g levels.[13] This D_{4h} configuration further splits the T_{2g} and E_g levels into E_g, B_{2g}, A_{1g}, and B_{1g}.

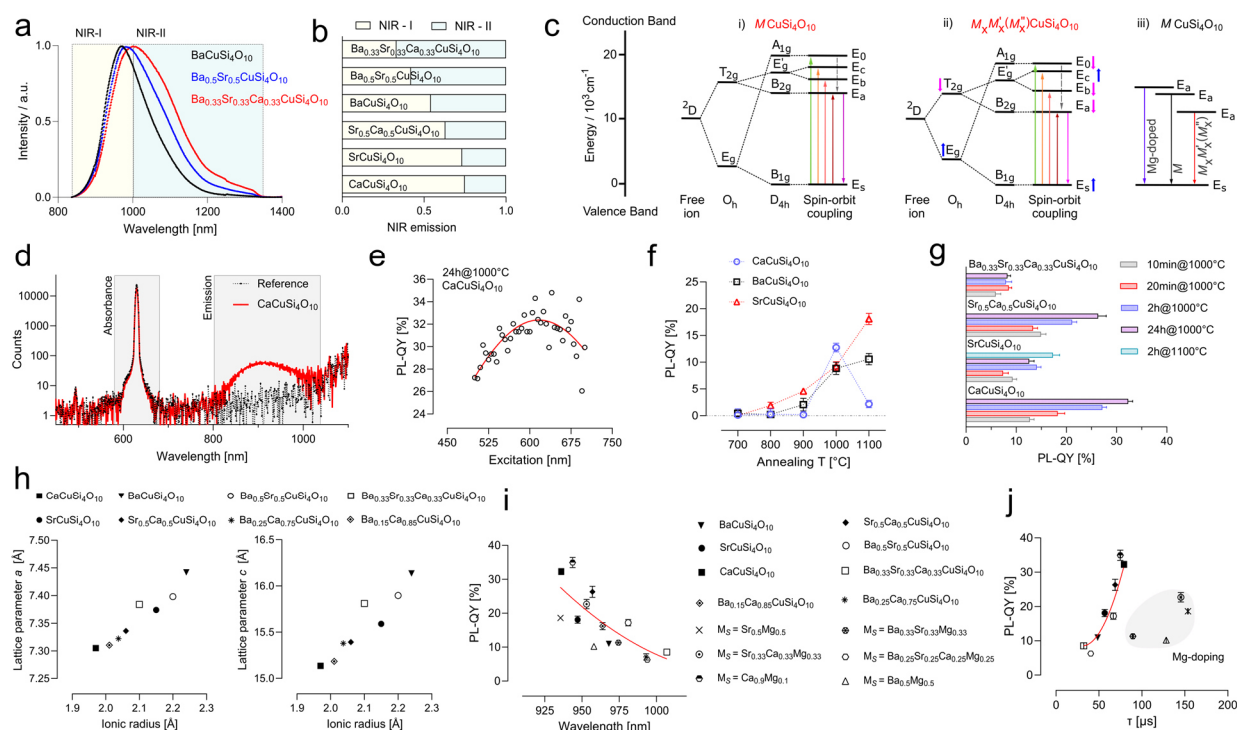**Figure 5: Photoluminescence engineering of copper tetrasilicates enables emission shift to NIR-II window.**
a) NIR emission spectrum of $BaCuSi_4O_{10}$ and its mixed forms showing a significant impact of (multi)element doping towards shifting the emission into the NIR-II window (>1000 nm). b) Evaluation of the NIR emission spectra as integrated for NIR-I (simplified as <1000 nm) and for NIR-II (>1000 nm). c) Simplified energy diagram of Cu^{2+} ion within a tetragonally distorted crystal field, for i) non-doped, single M-containing NS and ii) multielement doped NS, highlighting the shifted E_a energy levels (iii). d) Absolute photoluminescence quantum yield (PL-QY) spectra of $CaCuSi_4O_{10}$. Integrated photon counts within the gray box, excitation at 630 nm. e) PL-QY dependency on the excitation wavelengths (red line = Gaussian fit; PL-QY = 32%). f) PL-QY engineering through variation of annealing temperature of resynthesized copper tetrasilicates. g) PL-QY engineering through optimizing annealing time, showing a general trend of increasing PL-QY with prolonged annealing (mean ± SD). h) Correlation between the lattice parameter a and c, obtained from Rietveld refinement, and the calculated ionic radius of the (mixed) alkaline earth metal copper silicates. i) Correlation of the optimized PL-QY to the emission wavelengths of all synthesized 2D copper tetrasilicates variations (for comparison with reference values see Supplementary Figure S29, red line = second order polynomial fit). j) Correlation between the PL-QY and fluorescence lifetime of all obtained materials (red line = second order polynomial fit of non-Mg containing NS).

Additionally, strong spin-orbit coupling causes these energy levels to split further into five distinct levels: E_0, E_c, E_b, E_a, and E_s. As for the doped CTS structures, including the mixed forms between Sr-Ca, Ba-Sr, Ba-Ca and Ba-Sr-Ca a significant bathochromic shift in emission was detected, the E_a energy level needs to be downshifted for multi-doped CTSs (Figure 5cii). This could be caused by a more ordered CuO_4 tetrahedron, due to impacting the Cu-O bond lengths by replacing the alkaline earth metals within the 2D CTS structure.[26] As a consequence, the crystal field splitting of the O_h symmetry would be weakened, downshifting the T_{2g} level and upshifting the E_g level (Figure 5cii).[32,33] This would further influence the second splitting of the spin-orbit coupling, overall downshifting the E_a energy levels. Similarly, the E_a energy levels should increase due to Mg-doping, as seen for the blue-shifted emission of Mg-doped-$SrCuSi_4O_{10}$ and Mg-doped-$BaCuSi_4O_{10}$ (Figure 5ciii). In the next step, absolute quantum yield spectroscopy was employed to assess the performance and impact of multi-element doping on the emittance of the different CTSs. Figure 5d shows the PL-QY spectrum of $CaCuSi_4O_{10}$ whereas the area for absorbed and emitted photons are highlighted in gray. This direct and absolute method furthermore allows to evaluate the dependency of the PL-QY on the excitation wavelengths (Figure 5e), showing maximum emission when excited at 615-630 nm with a mean PL-QY of 32%. This is in agreement with the maximum of the respective UV-Vis-NIR absorption spectra (Supplementary Figure S28). Using this technique furthermore allows for the photoluminescence engineering of the NS, as optimization of annealing conditions seemed to impact the nanomaterial's emittance significantly. As shown in Figure 5f, different annealing temperatures modulated the PL-QY of the copper tetrasilicates in a different manner. Emission increases when annealing of the FSP-particles leads to the desired *P4/n c c* crystal phase and decreases, like in case of $CaCuSi_4O_{10}$ if excessive heating led to the degradation of such. However, in case of $SrCuSi_4O_{10}$ the PL-QY was found highest, when sintered at 1100°C even if structural parameters stayed the similar to the material sintered at 1000°C. In addition to it, also

the annealing time was found to drastically impact the PL-QY of some of the synthesized materials, such as seen for $CaCuSi_4O_{10}$ or $Sr_{0.5}Ca_{0.5}CuSi_4O_{10}$ (Figure 5g), where prolonged annealing improves the emission. For other chemical modification of the NS structures, such as $Ba_{0.33}Sr_{0.33}Ca_{0.33}CuSi_4O_{10}$ no significant enhancement could be found (Supplementary Figure S28). PL-QY of 2h annealed samples were found to be 16% for $Ba_{0.15}Ca_{0.85}CuSi_4O_{10}$ and 7% for $Ba_{0.25}Ca_{0.75}CuSi_4O_{10}$. This translates to a 50% increased emission of $Ba_{0.15}Ca_{0.85}CuSi_4O_{10}$ compared to undoped $BaCuSi_4O_{10}$, while exhibiting similar fluorescence emission features.

Finally, the structural and optical properties were analyzed across the different phases. Based on the Rietveld refinement of the XRD analysis, the lattice parameters *a* and *c* were plotted against the calculated ionic radii of the alkaline earth metal combinations (Figure 5h). For the newly synthesized Ba-Ca and Ba-Sr-Ca CTS combinations, a minor distortion of the crystal lattice becomes visible, as lattice parameter *c* is slightly shifted towards larger values. When comparing the optimized PL-QY and the emission wavelengths of each respective CTS, a contrasting trend becomes visible (Figure 5i). The PL-QY decreases with bathochromic shifted emission maxima, following an overall trend of a second order polynomial fit. When comparing the CTS's photoluminescence parameters with previous reports, it becomes evident that the FSP-synthesized CTS possesses on average significantly higher quantum yields (Supplementary Figure S29). Matching the PL-QY and fluorescence lifetime values resulted in two distinctive groups (Figure 5j). The majority of mixed CTS follow a trend, resembled by a second order polynomial fit ($R^2 = 0.92$) showing a simultaneous increase of both parameters. However, a second group with larger fluorescence lifetimes were observed, associated with Mg-doping of the respective CTS structures.

Brilliant nanosheets for super-resolution microcirculation mapping of the murine brain
After obtaining highly fluorescent CTS-NS with engineered emission wavelengths, we evaluated their performance as optical contrast agents for

macroscopic brain vasculature imaging. Widefield imaging of the murine brain was performed following intravenous (i.v.) injection of NS, ensuring a homogeneous distribution of NS in the brain vasculature within seconds. An 808 nm laser was used to excite the NS's B_{2g} energy transition located in the NIR-I window, while a short-wave infrared (SWIR) camera enabled large-scale detection of fluorescence emission across the entire cortex from ~20 cm distance above the mouse through the intact skull (Figure 6a). The dispersion of NS in water was found to be highly efficient for the FSP-derived CTS material, in contrast to the commercial counterpart, while maintaining a high fluorescence (Supplementary Figure S30). However, to enable in vivo colloidal stability of

the NS after i.v. injection, the surface of the particles was functionalized, as bare NS tended to aggregate in blood. We employed two straightforward strategies to coat the NS: modification with dimercaptosuccinic acid (DMSA) and PEGylation. Both approaches altered the surface charge to more negative values as seen by Zeta-potential measurements, while keeping the size distribution unchanged (Supplementary Figure S30c). An additional feature making these NS promising candidates for imaging applications is their significantly superior photostability compared to organic dyes. The synthesized NS, including the multielement doped ones, demonstrated resistance to photobleaching (Figure 6b).
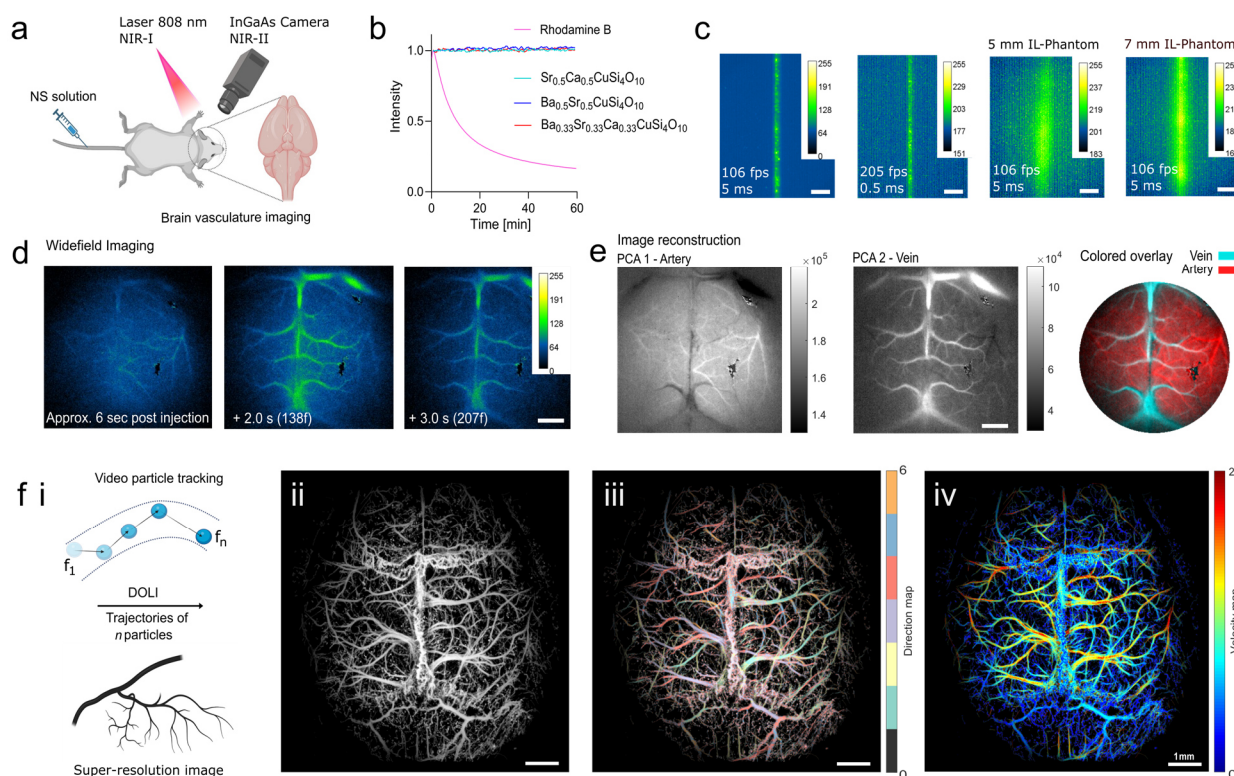

Figure 6: Engineered nanosheets for super-resolution mapping of the murine brain. a) Schematic of the diffuse optical localization imaging (DOLI) system used for cerebrovascular imaging in the NIR window. A SWIR camera was used to collect the fluorescence emission of a dispersion of stabilized NS injected intravenously (i.v.) under 808 nm excitation (850 mW/cm^2). b) Photostability of NSs compared to a common organic dye (Rhodamine B). c) High-frame-rate imaging of $CaCuSi_4O_{10}$ NS placed inside a vessel-mimicking Teflon tube (280 µm inner diameter). Light scattering of brain tissues was mimicked with a 1.2% intralipid (IL) phantom (scale bar = 500 µm). d) Time-lapse widefield images post DMSA-stabilized NS injection (scale bar = 500 µm). e) Veins and arteries could be differentiated based on principal component analysis (PCA) (scale bar = 500 µm). f) Schematic overview (i) of the working principle of DOLI rendering the structural (ii), blood flow direction (iii) and velocity (iv) maps of cerebral vasculature from continuous localization and tracking of circulating PEGylated NSs (scale bar = 1 mm).

High-frame-rate imaging of various NS perfused through a vasculature-mimicking microtubing served to determine the most optimal NS candidate. $CaCuSi_4O_{10}$ NS were found to exhibit a particularly prominent performance due to their brightest emission, allowing visualization with over 200 fps (Figure 6c) under light exposure conditions suitable for in vivo imaging. Blurring of the acquired fluorescence images was observed when an intralipid (IL) phantom simulating light scattering in brain tissues was placed above the microtubing, as evidenced by an enlarged point spread function (Figure 6c, right). More interestingly, i.v. injection of the NS in mice revealed that the surface modification can strongly impact their performance as contrast agents. Two phases were distinguished following i.v. injection of DMSA-stabilized NS. The bolus of particles first appeared to uniformly distribute across the vasculature in the collected images in a similar manner as a conventional fluorescent dye (Figure 6d). High-frame-rate imaging (69 fps) in this phase enabled differentiation of the vascular tree into veins and arteries, based on their different perfusion patterns (Figure 6e). This initial NS bolus was followed by dilution of the NS in blood, which resulted in dots distinguishable in the images corresponding to individual or small clusters of NS circulating in the bloodstream. This sparse distribution of circulating particles enabled their individual localization and tracking using the recently reported diffuse optical localization imaging (DOLI) method. By continuously tracking the trajectory of numerous particles, a super-resolution and background-free vascular image could be reconstructed (Figure 6fi). However, the DMSA functionalized NSs were found to circulate for less than a minute before getting cleared from the bloodstream, resulting in a fragmentary DOLI image (Supplementary Figure S31 On the contrary, PEGylated NS exhibited an extended circulation time, allowing to localize circulating particles even 10 min post injection. The reconstructed DOLI images (Figure 6f) then revealed cortex-wide brain vasculature networks in great detail (f*ii*). Beyond structural information, blood flow direction (f*iii*) and velocity (f*iv*) maps could be reconstructed,

allowing the NS to function as fluorescence-based velocity sensors in the NIR-II.

Nanosheet-labeled macrophages enable large-scale single-cell tracking

Inspired by the bright emission of trackable NS, we aimed to use them as a NIR-fluorescent label for immune cells, potentially enabling single-cell tracking within the macroscopic imaging system. However, for effective macrophage loading, the NS needed to be applied at the highest possible concentrations, which were determined within a cell viability assay, combined with a marker identifying cell membrane damage. As shown in Figure 7a, we compared undoped and multielement doped NS with bare SiO_2, identifying the CTS as generally more compatible. $CaCuSi_4O_{10}$ NS were found to exhibit minimal effects on cell viability up to a concentration of 100 ug/mL, whereas for $Ba_{0.33}Sr_{0.33}Ca_{0.33}CuSi_4O_{10}$ only half of the cells survived at the same concentration. Cell membrane damage followed a complementary trend, showing increased lactate-dehydrogenase (LDH) release with decreasing cell survival. Moreover, PEGylating the NS surface further improved cytocompatibility, compared to the non-functionalized NS (Supplementary Figure S32), making them a suitable candidate to boost the overall uptake. Extensive washing was applied, to remove NS not uptaken by the cells from the culture, while loaded macrophages were detached from the culture well surface and fixed as single-cell suspension, functioning as a carrier for the luminescent cargo. Figure 7b shows a (fluorescence) image of a single macrophage on a microscopic scale, that appears to internalize the NS likely via phagocytosis. When performing high-frame-rate imaging tests in the previously mentioned capillary system, single fluorescent spots were clearly visible, getting blurred underneath an intralipid tissue phantom (Supplementary Figure S33b). These cells were then re-injected into the mouse model for brain vasculature imaging. A snapshot of a moving cell is presented in Supplementary Figure S33c, demonstrating that the detected fluorescence signal was strong enough to enable tracking across multiple frames. This allowed us to capture

13

the trajectories of several cells, which remained visible at the cerebral scale for 5 - 40 frames, corresponding to less than one second at a frame rate of 69 fps. When these trajectories are plotted

and overlaid onto the high-resolution vascular image, it becomes clear that macrophage movement closely follows sections of the vascular tree (Figure 7c).
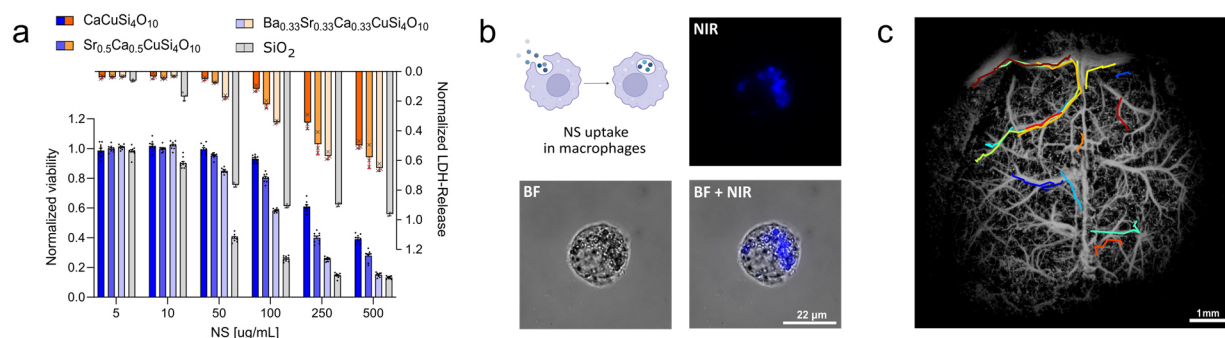

Figure 7: Individual macrophage tracking in vivo. a) Macrophage cell toxicity test for various NS comparted to SiO_2 (Aerosil 90; mean ± SD). b) Schematic representation of NSs uptaken by human macrophages, with respective bright field (BF) and NIR-fluorescence images of a single NS-labeled cell. c) Overlay of all tracked macrophages (N = 15) resemble parts of the vasculature tree (DOLI image from Supplementary Figure S31; scale bar = 1 mm).

Discussion

The development of new high-performance NIR-II contrast agents is set to significantly advance the diagnostic and therapeutic potential of non-invasive optical imaging and paves the way for molecular imaging. In this context, the introduced FSP-synthesis route offers a promising approach to compositionally engineer CTSs, creating highly fluorescent nanomaterials suited for bioimaging and biosensing. This modular FSP approach presents several advantages over previous synthesis methods, particularly in eliminating unwanted elements introduced during the synthesis process. By enabling the residual-free combustion of metal-organic precursors, this technique produces high-purity CTSs. In contrast, traditional methods such as the melt-flux technique rely on inorganic salts and flux agents like soda or plant ash to lower the melting point of silica, often leaving contaminants within the material. These contaminants can result in the formation of unwanted crystal phases, including a glassy background, which introduces defects at grain boundaries and diminishes the fluorescence properties of the nanomaterial.[34] Moreover, the FSP process can be scaled up to an industrial level, enabling the production of nanoparticles at rates ranging from hundreds of grams per hour to several kilograms per hour.[35] The FSP-derived

material itself enables precise study of temperature-dependent crystal phase transitions and their kinetics. For example, previous reports describe the formation of cuprorivaite powders taking several hours at 1000°C, annealing the primary FSP material yields CTSs within minutes. This suggests that with a homogeneous elemental distribution, the rearrangement into a 2D crystal lattice occurs approximately two orders of magnitude faster than previously documented.[13] This rapid process forms the basis for effective chemical doping strategies, as it significantly reduces the need for prolonged sintering times, thereby minimizing unwanted phase segregations. Future approaches could further refine this technique, potentially allowing for the bottom-up synthesis of low-dimensional NSs through uniform annealing within a circulating gas stream, avoiding excessive sintering of material clusters. Most interestingly on the way to NIR-emission engineered contrast agents, the FSP-synthesis allowed for the first time multi-alkaline earth metal doped CTSs. Uniting Ba and Ca, and Ba, Sr and Ca within the lattice structure was observed to shift PL emission into the NIR-II spectral window. Such shift could be attributed to modulation a of the square-planar coordinated Cu^{2+} in the distorted crystal field, as expansion of the Cu−O bond length and more

ordering of the CuO_4 tetrahedron could occur, resulting in a lowered transition energy of the doped-NS.[26] Previous studies found, that exchange of cations seems to induce a change in the crystal field environment around Cu^{2+} ions, impacting the emission wavelength, however only comparing updoped MCuSi$_4$O$_{10}$.[36] As strongest bathochromic PL shifts were detected in meta-stable NS that unite Ca and Ba in the crystal lattice, we hypnotize, that the substantial change in Ca-O and Ba-O bond lengths (~0.4 Å)[31], could partly explain the weakening of the crystal field and hence the dramatic shift in fluorescence emission. Moreover, slight doping of the crystal lattice with Mg was achieved. While this doping does not significantly alter the overall lattice parameters, it does induce a noticeable shift in photoluminescence emission towards higher energies and an accompanying increase in fluorescence lifetime. This hypsochromic shift in emission aligns with the modulation of Mg-O bond lengths, as the shorter Mg-O bonds could strengthen the crystal field, thereby increasing the transition energy in the Mg-doped CTSs. Building on these findings, we have developed a new series of optically active materials, which hold potential for use as multi-color NIR-fluorescent lifetime labels in future applications. We overall present a comprehensive set of CTS structures, enabling robust comparison of their optical properties. This foundational work expands the range of available NIR-emission tailored materials, as the FSP synthesis approach opens avenues for studying additional multi-element systems. This includes the substitution of ions like Zn or La, and the development of functional hybrid structures.[37] Streamlining the FSP process into an automated, AI-driven, continuous synthesis platform could facilitate rapid and effective screening of engineered nanostructures in the future, extending applications beyond merely improving emission properties.[38,39] By accessing highly fluorescent nanostructures and applying biocompatible surface modifications, the engineered NS were successfully employed as in vivo contrast agents in an animal model. To the best of our knowledge, this represents the first reported in vivo bioimaging application for the entire class of CTS

materials. This achievement demonstrates the potential applications beyond insect systems,[10] showing that small, highly luminescent particles can be obtained without the need for elaborate mechanical degradation of bulk CTS material, known to significantly degrade PL emission and obstruct bioimaging applications.[22] Previously, NIR-emitting QDs containing heavy metals have been used to reconstruct blood flow velocity,[4] and similarly, for DOLI-based super-resolution image reconstruction.[40] CTS-NS could provide a heavy metal-free alternative, with the added capability of imaging fine skull vessels. Advancements in the optical detection setup could even enable depth-resolved 3D localization and imaging.[41] By targeted functionalization of the NS surface with cell receptor binding units or antibodies, highly specific molecular imaging could be achieved, advancing from in vitro systems to in vivo cancer models.[42] The bright emission and biocompatibility of the synthesized NS were further demonstrated through their uptake by macrophages and subsequent in vivo tracking. To the best of our knowledge, this represents the first instance that single immune cells have been imaged in vivo, in real-time, on a cortex-wide scale. This lays the foundation for functional and molecular imaging with the proposed approach, including the labeling of other immune cells like T-cells to track their interactions with malignant tumors or to explore their roles within the tumor microenvironment. Beyond their potential application in biomedical imaging, these engineered CTS could be utilized in light-emitting devices, such as those for telecommunication platforms, as security inks, or luminescent solar concentrators. In conclusion, this work employs the tunable synthesis approach of flame-spray-pyrolysis to develop highly fluorescent, emission-engineered NSs, well-suited for next-generation in vivo bioimaging. The successful transcranial mapping of cortical microcirculation in mice and the tracking of immune cells across the cerebral region further highlights the promise of FSP-synthesized 2D-CTS as powerful NIR-II emissive agents for advanced bioimaging and beyond.

Material and Methods

Chemicals

All materials, if not stated otherwise, were purchased from Sigma–Aldrich or VWR Chemicals.

Flame-Spray-Pyrolysis

Organic precursor solutions were prepared to match the elemental composition of the desired copper tetrasilicate, hence a ratio of M:Cu:Si was set at 1:1:4 with M = Ca, Sr, Ba or Mg. Metal-Acetate precursors were dissolved in 2-ethylhexanoic acid (2-EHA) for 2h at 130 °C while constant stirring under reflux. Borchers® Deca Copper 8 was used as Cu precursor and Hexamethyldisilane as Si precursor. Conditions for a typical batch are given in the Supplementary Table 2. Metal-organic precursor solution in 2-EHA:THF (1:1) was injected through a needle into CH_4/O_2 flame (5 mL/min liquid-feed precursor stream; 5 L/min O_2; 3 L/min CH_4) and resulting nanoparticles were collected with a fine glass fiber filter located 70 cm above the flame and sieved through a 200 μm mesh. Annealing of the nanomaterial was performed between 700 - 1100°C for 10 min, using a TGA (METTLER TOLEDO TGA/DSC 3+; 25 k/min ramp; 40 ml/min air flow) or at ambient atmosphere for 2 – 24h at 900 -1100 °C (Sintering furnace Type 4800, Thermolyne).

Photoluminescence Spectroscopy

NIR fluorescence emission spectra were recorded with a Shamrock 193i spectrometer equipped with an InGaAs detector (Andor Technology Ltd., Belfast, Northern Ireland) using a 561 nm Cobolt Jive laser (Cobolt AB, Solna, Sweden) as excitation source. A monochromator (MSH150 instrument, equipped with a LSE341 light source, LOT-Quantum Design GmbH, Darmstadt, Germany) was used for excitation (5 nm steps) to obtain 2D-NIR excitation-emission spectra. In addition, NIR fluorescence emission spectra were recorded with a NIRQuest+1.7 spectrometer (InGaAs detector, OceanOptics), fiber-coupled to a customized Axiovert 40CFL using a 10x objective, 800 nm dichroic mirror (Edmund optics) and 900 nm LP filter (FELH0900, Thorlabs). Excitation was performed with a fiber-coupled 750 nm CW laser (FC-750-5W, CNI, China). Absolute photoluminescence quantum yield (PL-QY) spectroscopy was performed with a Hamamatsu Quanturus-QY (C11347-12) using solid phase quartz glass sample holders. Excitation scan regime was set to 500-700 nm (seps of 5 nm), while the area to detect all emitted photons was adjusted to cover the entire emission, e.g. for typically from 500-700 nm in steps of 5 nm, using the spectrometer software to calculate the PL-QY.

Fluorescence Microscopy

For NIR fluorescence photobleaching experiments, fluorescence microscopy was performed using a custom-made setup containing a 561 nm laser (Jive 500, Cobolt AB, Sweden) and an inverted microscope (IX73, Olympus, Japan) equipped with a 20x objective (MPlanFL N 20, Olympus, Japan). The fluorescence signal was split using a dichroic mirror (R785, AHF Analysentechnik, Germany) and the fluorescence then was captured using two cameras, a cMOS camera (Andor Zyla 5.5, Oxford Instruments, UK) for visible range signals and an InGaAs camera (Xeva 1.7-320, Xenics, Belgium) for NIR signals. Photobleaching was tested with dispersed NS (1 mg/ml in H_2O) and Rhodamine B (1 mg/ml in H_2O). 100 μl of the dispersions/solutions were put on glass bottom petri dishes, dried and imaged at 400 mW excitation power every 15 s for 1 h. The fluorescence intensity corresponds to the mean gray value of averaged over 5 imaged nanoparticles imaged by the NIR camera (NS) or the mean gray value of the complete illuminated area imaged by the VIS camera (Rhodamine B), each after background correction.

Fluorescence Lifetime measurements

For fluorescence lifetime measurements in the frequency domain, a fiber-optic oxygen sensor (FireSting O_2, PyroScience, Germanay) was used.[20] The sensor emits light with an excitation wavelength of 620 nm; allowing for modulation of the excitation frequency between 100 - 16000 Hz and detects induced fluorescence. The phase shift between the excitation signal and the detected fluorescence was extracted from the sensor raw data to calculate fluorescence

lifetimes. Measurements were performed on dry samples, with the FireSting optical probe mechanically positioned at a fixed distance from the sample of a few milligrams sample powder placed in a reaction tube. Measurements were conducted at constant conditions and settings (excitation frequency: 4000 Hz, LED intensity: 60 %, amplification factor: 400x, signal intensity ~ 14 mV). Each sample was measured for 1 min at 1 fps.

X-ray diffraction (XRD)

X-ray diffraction measurements (XRD) were performed with a Bruker D2 2nd Gen Phaser (30 kV, 10 mA, SSD160 detector, Cu tube 1.54184 [Å] Kα radiation at $2\theta = 10°-80°$ with a step size of 0.01°). For Rietveld analysis, additional XRD measurements were performed at room temperature on a Malvern PanAlytical X`Pert Powder instrument in Bragg-Brentano geometry with Ni-filtered Cu Kα radiation (λ=1.5418 Å). The powders were grinded before measurement and the diffraction patterns were acquired in an angular range of 5-120° 2Ө with a measurement time of 19 hours per sample. Additional phases besides the expected main 'P4/ncc' tetragonal phase were identified with the *Search&Match* option within the software X'Pert HighScore.[43] Rietveld analysis with the identified phases was performed using the software TOPAS.[44] The crystallographic information files (CIFs) for the refinement were retrieved from the Inorganic Crystal Structure Database (ICSD).[45] For the identified phases, Supplementary Table 3 lists the mineral name, chemical formula, crystal system, space group and ICSD code. Besides the lattice parameters, the scale factors defining the Rietveld quantification and peak shapes were modelled with the Thompson-Cox-Hastings pseudo-Voigt (TCHZ) model. Preferred orientation in the main '*P4/ncc'* phase was accounted for with spherical harmonics. Retrieved lattice parameters and quantification are given in the Supporting Information. It should be noted that the estimated standard deviations (σ) on these parameters from Rietveld refinement represent rather the precision of these parameters than the accuracy[46] and the estimated probable error is rather 2-3 σ .[47,48] Further, we routinely measure a silicon standard

after any configurational changes of the diffractometer. We observe a deviation in the peak position of the (004)-reflection of 0.003° 2Ө within the time frame in which the here presented samples have been investigated, which would represent the uncertainty related to the instrumental setup.

Electron microscopy

Scanning electron microscopy (SEM) combined with energy-dispersive X-ray spectroscopy (EDX) was conducted using an Axia Chemisem (Thermo Fisher, NL). Prior to analysis, the samples were coated with a 10 nm layer of carbon using a Leica EM ACE600. For transmission electron microscopy (TEM) analysis, nanoparticles were drop-cast onto nickel grids (EMR, Holey Carbon Film 300 Mesh), air-dried, and imaged at various magnifications with a Zeiss EM 900 microscope (Carl Zeiss Microscopy GmbH, Germany) operating at 80 kV. Particle size distributions were determined using ImageJ (version 1.54b). These grids were further examined with high-angle annular dark-field (HAADF) scanning transmission electron microscopy (STEM) paired with energy-dispersive X-ray spectroscopy (EDX) on a Talos F200X TEM microscope (FEI), utilizing four detector configurations (Super-X EDS) at 200 kV.

Nanosheet dispersion and surface modification

Typically, 50 mg NP were grinded with a mortar and dispersed in H_2O (5 mg/mL, 3 min 90% amplitude, Sonics Vibra cell VCX 500, cup horn) followed by 3 min cup-horn sonication (Sonics Vibra cell VCX 500, CV334 converter). Surface modification with meso-2,3-Dimercaptosuccinic acid (DMSA) and via PEGylation was performed by adapting a previously reported protocol.[49] Surface grafting with DMSA follows a previous description.[50] In brief, 50 mg of respective CTS material were dispersed in 10 mL of water, followed by the addition of 15 mL of DMSA solution (1 mg/mL in H_2O). To ensure complete dissolution, the DMSA solution was gently heated prior to addition. The resulting mixture was stirred at 300 rpm for 2.5h at RT, then centrifuged at 7100 rpm for 20 minutes. After

17

discarding the supernatant, the pellet was redispersed in 25 mL of H_2O, and the pH was adjusted to 10 using NaOH while stirring at 300 rpm for 1h. Finally, the pH was lowered to 7.3, and the mixture was stored at RT. NS fraction was collected as the supernatant after 6h of sedimentation. For PEGylation, 100 mg of CTS particles were dispersed in 30 mL of ethanol (10 min 95% amplitude, Sonics Vibra cell VCX 500, cup horn), followed by the addition of 1 mL of PEG-1000-Si and 100 μL of 32% ammonia solution, based on a reported synthesis protocol for PEG-silane coupling and subsequent silica nanoparticle modification.[51] This mixture was heated under reflux at 75°C for 24 hours. The resulting nanoparticles were centrifuged (10 min, 5000x g) and sequentially washed with 20 mL each of H_2O, ethanol, THF, ethanol, and H_2O. The PEGylated material was then dispersed in H_2O for further use, with the NS fraction collected as the supernatant after 30 minutes of sedimentation.

Nanoparticle Characterization

Hydrodynamic size measurements via dynamic light scattering (DLS) and zeta potential determination were conducted using a Zetasizer Nano-ZS (Malvern Instruments). The surface area was measured using the Brunauer–Emmett–Teller (BET) method at 77 K with a Micromeritics Tristar II Plus.

Cell experiments

Human Monocytes (THP-1, ATCC) were cultured in standard conditions at 37 °C in a humidified atmosphere containing 5 % CO2 and sub-cultured at 70% confluency. In vitro nanomaterial toxicity and viability of macrophages after 24 h nanomaterial incubation was performed using the LDH-release (G1780, Promega) and ATP quantification CellTiter-Glo® luminescence assay (G7570, Promega), respectively. In brief, 40,000 THP-1 cells in 100 uL RPMI-1640-Medium (R8758, Sigma-Aldrich, supplemented with 10% FCS, 1% l-glutamine, 1% Penicillin-Streptomycin) and 200 nM PMA were seeded in black 96 well plates with transparent bottom. After 3 days, the cell medium of the differentiated macrophages was replaced

with PMA-free cell medium. One day after, the cell medium was exchanged with nanomaterial containing cell medium or the vehicle control medium. All conditions contained 10% milliQ water. After 24 h nanomaterial incubation 50 uL of supernatant was used for LDH-release quantification. The assay was performed according to the manufacturer's specifications. For the viability assay, the remaining cell medium was exchanged with fresh cell medium and CellTiter-Glo® reagent was added (1:1). After 10 min shaking in the dark, luminescence was quantified using a microplate reader (Berthold LB-943). For macrophage loading with NS, 1 million cells were initially seeded into 6-well plates in 3 mL cell medium containing 200 nM PMA. The cell medium was replaced with PMA-free cell medium 3 days after. The next day, nanomaterials solutions were added reaching the desired concentration and a maximum of 10% H_2O content. A concentration of 200 μg/mL PEGylated NS was used to label cells for later in vivo tracking experiments. After 24 h nanomaterial incubation, cells were washed twice using PBS and then trypsinized using TrypLE. Additionally, cells were fully detached using a cell scraper. Thereafter, cells were fixed at room temperature using 4% PFA, creating a single-cell solution. After washing away PFA using PBS twice, fixed and NS-loaded cells were suspended in PBS containing 1mM EDTA.

Animals

Athymic nude-Foxn1nu mice (N = 4; Envigo BMS B.V., Netherlands) were used for in vivo cerebral microcirculation imaging. The mice were housed in ventilated cages with ad libitum access to food and water. The housing room was kept under a 12 h dark/light cycle, 22 °C room temperature, and ~50% relative humidity. All animal experiments were performed in accordance with the Swiss Federal Act on Animal Protection and approved by the Cantonal Veterinary Office Zurich. For in vivo imaging, the mice were anesthetized with isoflurane (5% for induction and 1.5% for maintenance) in a mixture of O_2 and medical air with flow rates of 0.2 L/min and 0.8 L/min, respectively. For transcranial imaging, the scalp of mouse was

removed post subcutaneous injection of analgesics (Buprenorphine, 0.1 mg/kg). Widefield recording was performed during and after intravenous injection of 100 uL NS solution (10 mg/mL) for a total duration of 10 min. In vivo single-cell tracking was realized by injecting a total volume of 100 uL PBS solution, containing about 8000 NS-loaded macrophages per uL.

Diffuse optical localization imaging (DOLI) in the NIR-II window

DOLI was performed with a custom-built widefield microscope, as described in detail previously.[40] Briefly, an 808 nm CW laser (FC-808-20W, CNI, China) with fiber output was employed to provide epi-illumination on the sample, with beam size adjustable with a collimator (CNI, China). The fluorescence emission was then collected by the camera lens (LM50HCSW, Kowa, Japan), filtered with a 950 nm long-pass filter (FELH0950, Thorlabs, USA), focused on the InGaAs-based SWIR camera (WiDy SenS 640V-ST, NiT, France). The collected widefield image stack was processed using a localization-based image reconstruction pipeline, as previously described.[40] Here, each frame was first denoised, followed by the localization of individual moving particles. These particles were subsequently tracked across the image stack using u-track algorithm.[52] Both the localization and tracking were performed using the open-source TrackNTrace toolbox.[53] The trajectories derived from the tracking algorithm provided additional functional information, such as flow velocity and direction at a given frame rate. By superimposing the particle count/flow velocity/direction at each pixel, the structural/flow velocity/direction maps of brain vasculature were rendered accordingly. Similar imaging conditions were used for visualization of NS-loaded macrophages. Image analysis for macrophages tracking was performed using background-subtracted images in TrackMate (v7.10.2), ImageJ (1.54).

References

(1) Wang, F.; Zhong, Y.; Bruns, O.; Liang, Y.; Dai, H. In Vivo NIR-II Fluorescence Imaging for Biology and Medicine. *Nat. Photonics* **2024**. https://doi.org/10.1038/s41566-024-01391-5.

(2) Hong, G.; Antaris, A. L.; Dai, H. Near-Infrared Fluorophores for Biomedical Imaging. *Nat. Biomed. Eng.* **2017**, *1* (1), 0010. https://doi.org/10.1038/s41551-016-0010.

(3) Bandi, V. G.; Luciano, M. P.; Saccomano, M.; Patel, N. L.; Bischof, T. S.; Lingg, J. G. P.; Tsrunchev, P. T.; Nix, M. N.; Ruehle, B.; Sanders, C.; Riffle, L.; Robinson, C. M.; Difilippantonio, S.; Kalen, J. D.; Resch-Genger, U.; Ivanic, J.; Bruns, O. T.; Schnermann, M. J. Targeted Multicolor in Vivo Imaging over 1,000 Nm Enabled by Nonamethine Cyanines. *Nat. Methods* **2022**, *19* (3), 353–358. https://doi.org/10.1038/s41592-022-01394-6.

(4) Bruns, O. T.; Bischof, T. S.; Harris, D. K.; Franke, D.; Shi, Y.; Riedemann, L.; Bartelt, A.; Jaworski, F. B.; Carr, J. A.; Rowlands, C. J.; Wilson, M. W. B.; Chen, O.; Wei, H.; Hwang, G. W.; Montana, D. M.; Coropceanu, I.; Achorn, O. B.; Kloepper, J.; Heeren, J.; So, P. T. C.; Fukumura, D.; Jensen, K. F.; Jain, R. K.; Bawendi, M. G. Next-Generation in Vivo Optical Imaging with Short-Wave Infrared Quantum Dots. *Nat. Biomed. Eng.* **2017**, *1* (4). https://doi.org/10.1038/s41551-017-0056.

(5) Zhang, M.; Yue, J.; Cui, R.; Ma, Z.; Wan, H.; Wang, F.; Zhu, S.; Zhou, Y.; Kuang, Y.; Zhong, Y.; Pang, D. W.; Dai, H. Bright Quantum Dots Emitting at ~1,600 Nm in the NIR-IIb Window for Deep Tissue Fluorescence Imaging. *Proc. Natl. Acad. Sci. U. S. A.* **2018**, *115* (26), 6590–6595. https://doi.org/10.1073/pnas.1806153115.

(6) Cao, J.; Zhu, B.; Zheng, K.; He, S.; Meng, L.; Song, J.; Yang, H. Recent Progress in NIR-II Contrast Agent for Biological Imaging. *Front. Bioeng. Biotechnol.* **2020**, *7* (January), 1–21. https://doi.org/10.3389/fbioe.2019.00487.

(7) Hong, G.; Diao, S.; Chang, J.; Antaris, A. L.; Chen, C.; Zhang, B.; Zhao, S.; Atochin, D. N.; Huang, P. L.; Andreasson, K. I.; Kuo, C. J.; Dai, H. Through-Skull Fluorescence Imaging of the Brain in a New near-Infrared Window. *Nat. Photonics* **2014**, *8* (9), 723–730. https://doi.org/10.1038/nphoton.2014.166.

(8) Zhong, Y.; Ma, Z.; Wang, F.; Wang, X.; Yang, Y.; Liu, Y.; Zhao, X.; Li, J.; Du, H.; Zhang, M.; Cui,

Q.; Zhu, S.; Sun, Q.; Wan, H.; Tian, Y.; Liu, Q.; Wang, W.; Garcia, K. C.; Dai, H. In Vivo Molecular Imaging for Immunotherapy Using Ultra-Bright near-Infrared-IIb Rare-Earth Nanoparticles. *Nat. Biotechnol.* **2019**, *37* (11), 1322–1331. https://doi.org/10.1038/s41587-019-0262-4.

(9) Lei, Z.; Zhang, F. Molecular Engineering of NIR-II Fluorophores for Improved Biomedical Detection. *Angew. Chemie - Int. Ed.* **2021**, *60* (30), 16294–16308. https://doi.org/10.1002/anie.202007040.

(10) Selvaggio, G.; Chizhik, A.; Nißler, R.; Kuhlemann, Ilyas; Meyer, D.; Vuong, L.; Preiß, H.; Herrmann, N.; Mann, F. A.; Lv, Z.; Oswald, T. A.; Spreinat, A.; Erpenbeck, L.; Großhans, J.; Karius, V.; Janshoff, A.; Pablo Giraldo, J.; Kruss, S. Exfoliated near Infrared Fluorescent Silicate Nanosheets for (Bio)Photonics. *Nat. Commun.* **2020**, *11* (1), 1–11. https://doi.org/10.1038/s41467-020-15299-5.

(11) He, C.; Dong, C.; Yu, L.; Chen, Y.; Hao, Y. Ultrathin 2D Inorganic Ancient Pigment Decorated 3D-Printing Scaffold Enables Photonic Hyperthermia of Osteosarcoma in NIR-II Biowindow and Concurrently Augments Bone Regeneration. *Adv. Sci.* **2021**, *8* (19), 1–10. https://doi.org/10.1002/advs.202101739.

(12) Johnson-Mcdaniel, D.; Barrett, C. A.; Sharafi, A.; Salguero, T. T. Nanoscience of an Ancient Pigment. *J. Am. Chem. Soc.* **2013**, *135* (5), 1677–1679. https://doi.org/10.1021/ja310587c.

(13) Nicola, M.; Gobetto, R.; Masic, A. *Egyptian Blue, Chinese Blue, and Related Two-Dimensional Silicates: From Antiquity to Future Technologies. Part A: General Properties and Historical Uses*; Springer International Publishing, 2023; Vol. 34. https://doi.org/10.1007/s12210-023-01153-5.

(14) Hong, G.; Diao, S.; Antaris, A. L.; Dai, H. Carbon Nanomaterials for Biological Imaging and Nanomedicinal Therapy. *Chem. Rev.* **2015**, *115* (19), 10816–10906. https://doi.org/10.1021/acs.chemrev.5b00008.

(15) Accorsi, G.; Verri, G.; Bolognesi, M.; Armaroli, N.; Clementi, C.; Miliani, C.; Romani, A. The Exceptional Near-Infrared Luminescence Properties of Cuprorivaite (Egyptian Blue). *Chem. Commun.* **2009**, No. 23, 3392–3394. https://doi.org/10.1039/b902563d.

(16) Selvaggio, G.; Kruss, S. Preparation, Properties and Applications of near-Infrared Fluorescent Silicate Nanosheets. *Nanoscale* **2022**, *14* (27), 9553–9575. https://doi.org/10.1039/d2nr02967g.

(17) Chen, Y.; Shang, M.; Wu, X.; Feng, S. Hydrothermal Synthesis, Hierarchical Structures and Properties of Blue Pigments SrCuSi4O10 and BaCuSi4O10. *CrystEngComm* **2014**, *16* (24), 5418–5423. https://doi.org/10.1039/c3ce42394h.

(18) Borisov, S. M.; Würth, C.; Resch-Genger, U.; Klimant, I. New Life of Ancient Pigments: Application in High-Performance Optical Sensing Materials. *Anal. Chem.* **2013**, *85* (19), 9371–9377. https://doi.org/10.1021/ac402275g.

(19) Nißler, R.; Bader, O.; Dohmen, M.; Walter, S. G.; Noll, C.; Selvaggio, G.; Groß, U.; Kruss, S. Remote near Infrared Identification of Pathogens with Multiplexed Nanosensors. *Nat. Commun.* **2020**, *11* (1), 5995. https://doi.org/10.1038/s41467-020-19718-5.

(20) Selvaggio, G.; Weitzel, M.; Oleksiievets, N.; Oswald, T. A.; Nißler, R.; Mey, I.; Karius, V.; Enderlein, J.; Tsukanov, R.; Kruss, S. Photophysical Properties and Fluorescence Lifetime Imaging of Exfoliated Near-Infrared Fluorescent Silicate Nanosheets. *Nanoscale Adv.* **2021**, *3* (15), 4541–4553. https://doi.org/10.1039/d1na00238d.

(21) Hill, B.; Abraham, S.; Akhtar, A.; Selvaggio, G.; Tschulik, K.; Kruss, S. Surfactant Assisted Exfoliation of near Infrared Fluorescent Silicate Nanosheets. *RSC Adv.* **2023**, *13* (30), 20916–20925. https://doi.org/10.1039/d3ra04083f.

(22) Cai, Y.; Peng, W.; Song, Q.; Pluta, D.; Peppersack, C.; Breitung-Faes, S.; Kwade, A.; Bigall, N. C.; Vana, P. Nanoengineering of Egyptian Blue Nanosheets: Advantages and Limitations for Near-Infrared Photoluminescence Applications. *ACS Appl. Opt. Mater.* **2023**, *1* (1), 465–472. https://doi.org/10.1021/acsaom.2c00114.

(23) Athanassiou, E. K.; Grass, R. N.; Stark, W. J. Chemical Aerosol Engineering as a Novel Tool for Material Science: From Oxides to Salt and Metal Nanoparticles. *Aerosol Sci. Technol.* **2010**, *44* (2), 161–172. https://doi.org/10.1080/02786820903449665.

(24) Meierhofer, F.; Mädler, L.; Fritsching, U. Nanoparticle Evolution in Flame Spray Pyrolysis—Process Design via Experimental and Computational Analysis. *AIChE J.* **2020**, *66* (2), 1–14. https://doi.org/10.1002/aic.16885.

(25) Pokhrel, S.; Mädler, L. Flame-Made Particles for Sensors, Catalysis, and Energy Storage Applications. *Energy and Fuels* **2020**, *34* (11), 13209–13224. https://doi.org/10.1021/acs.energyfuels.0c02220.

(26) Huang, W.; Zhang, J.; Fan, J.; Chen, P.; Zhou, L.; Zhang, X. From Ancient Blue Pigment to Unconventional NIR Phosphor: A Thermal-Stable Near-Infrared I/II Broadband Emission from Ca1-XSrxCuSi4O10 Solid Solution. *Inorg. Chem.* **2024**, *63* (1), 812–823. https://doi.org/10.1021/acs.inorgchem.3c03811.

(27) Obata, K.; Konishi, R.; Okagami, A.; Matsushima, S. Effect of Ca Addition on Near-Infrared Reflection of SrCuSi4O10. *Chem. Lett.* **2024**, *53* (2), 1–5. https://doi.org/10.1093/chemle/upad026.

(28) Knight, K. S.; Henderson, C. M. B. Structural Basis for the Anomalous Low-Temperature Thermal Expansion Behaviour of the Gillespite-Structured Phase Ba0.5Sr0.5CuSi4O10. *Eur. J. Mineral.* **2007**, *19* (2), 189–200. https://doi.org/10.1127/0935-1221/2007/0019-1711.

(29) Knight, K. S.; Henderson, C. M. B. C. Structural Variations in the Wesselsiteeffenbergerite (Sr1xBaxCuSi4O10) Solid Solution. *Eur. J. Mineral.* **2010**, *22* (3), 411–423. https://doi.org/10.1127/0935-1221/2010/0022-2025.

(30) Qin, J.; Liu, Z.; Ma, M.; Liu, F.; Qi, Z. M.; Li, Y. Structure and Microwave Dielectric Properties of Gillespite-Type ACuSi4O10(A = Ca, Sr, Ba) Ceramics and Quantitative Prediction of the Q × f Value via Machine Learning. *ACS Appl. Mater. Interfaces* **2021**, *13* (15), 17817–17826. https://doi.org/10.1021/acsami.1c01909.

(31) Kendrick, E.; Kirk, C. J.; Dann, S. E. Structure and Colour Properties in the Egyptian Blue Family,

M1-XM′xCuSi4O10, as a Function of M, M′ Where M, M′ = Ca, Sr and Ba. *Dye. Pigment.* **2007**, *73* (1), 13–18. https://doi.org/10.1016/j.dyepig.2005.10.006.

(32) Li, Y. J.; Ye, S.; Wang, C. H.; Wang, X. M.; Zhang, Q. Y. Temperature-Dependent near-Infrared Emission of Highly Concentrated Cu2+ in CaCuSi4O10 Phosphor. *J. Mater. Chem. C* **2014**, *2* (48), 10395–10402. https://doi.org/10.1039/c4tc01966k.

(33) Chen, W.; Shi, Y.; Chen, Z.; Sang, X.; Zheng, S.; Liu, X.; Qiu, J. Near-Infrared Emission and Photon Energy Upconversion of Two-Dimensional Copper Silicates. *J. Phys. Chem. C* **2015**, *119* (35), 20571–20577. https://doi.org/10.1021/acs.jpcc.5b04819.

(34) Nicola, M.; Garino, C.; Mittman, S.; Priola, E.; Palin, L.; Ghirardello, M.; Damagatla, V.; Nevin, A.; Masic, A.; Comelli, D.; Gobetto, R. Increased NIR Photoluminescence of Egyptian Blue via Matrix Effect Optimization. *Mater. Chem. Phys.* **2024**, *313* (December 2023), 128710. https://doi.org/10.1016/j.matchemphys.2023.128710.

(35) Gröhn, A. J.; Pratsinis, S. E.; Sánchez-Ferrer, A.; Mezzenga, R.; Wegner, K. Scale-up of Nanoparticle Synthesis by Flame Spray Pyrolysis: The High-Temperature Particle Residence Time. *Ind. Eng. Chem. Res.* **2014**, *53* (26), 10734–10742. https://doi.org/10.1021/ie501709s.

(36) Pozza, G.; Ajò, D.; Chiari, G.; De Zuane, F.; Favaro, M. Photoluminescence of the Inorganic Pigments Egyptian Blue, Han Blue and Han Purple. *J. Cult. Herit.* **2000**, *1* (4), 393–398. https://doi.org/10.1016/S1296-2074(00)01095-5.

(37) Jose, S.; Reddy, M. L. Lanthanum-Strontium Copper Silicates as Intense Blue Inorganic Pigments with High near-Infrared Reflectance. *Dye. Pigment.* **2013**, *98* (3), 540–546. https://doi.org/10.1016/j.dyepig.2013.04.013.

(38) Szymanski, N. J.; Rendy, B.; Fei, Y.; Kumar, R. E.; He, T.; Milsted, D.; McDermott, M. J.; Gallant, M.; Cubuk, E. D.; Merchant, A.; Kim, H.; Jain, A.; Bartel, C. J.; Persson, K.; Zeng, Y.; Ceder, G. An Autonomous Laboratory for the Accelerated Synthesis of Novel Materials. *Nature* **2023**, *624* (7990), 86–91. https://doi.org/10.1038/s41586-023-06734-w.

(39) Ryu, B.; Wang, L.; Pu, H.; Chan, M. K. Y.; Chen, J. Understanding, Discovery, and Synthesis of 2D Materials Enabled by Machine Learning. *Chem. Soc. Rev.* **2022**, *51* (6), 1899–1925. https://doi.org/10.1039/d1cs00503k.

(40) Zhou, Q.; Chen, Z.; Robin, J.; Deán-Ben, X.-L.; Razansky, D. Diffuse Optical Localization Imaging for Noninvasive Deep Brain Microangiography in the NIR-II Window. *Optica* **2021**, *8* (6).

(41) Zhou, Q.; Nozdriukhin, D.; Chen, Z.; Glandorf, L.; Hofmann, U. A. T.; Reiss, M.; Tang, L.; Deán-ben, X. L.; Razansky, D. Depth-Resolved Localization Microangiography in the NIR-II Window. *Adv. Sci.* **2023**, *2204782*, 1–9. https://doi.org/10.1002/advs.202204782.

(42) Selvaggio, G.; Herrmann, N.; Hill, B.; Dervişoğlu, R.; Jung, S.; Weitzel, M.; Dinarvand, M.; Stalke, D.; Andreas, L.; Kruss, S. Covalently Functionalized Egyptian Blue Nanosheets for Near-Infrared Bioimaging. *ACS Appl. Bio Mater.* **2023**, *6* (1), 309–317. https://doi.org/10.1021/acsabm.2c00872.

(43) Degen, T.; Sadki, M.; Bron, E.; König, U.; Nénert, G. The High Score Suite. *Powder Diffr.* **2014**, *29* (August), S13–S18. https://doi.org/10.1017/S0885715614000840.

(44) Coelho, A. A. TOPAS and TOPAS-Academic: An Optimization Program Integrating Computer Algebra and Crystallographic Objects Written in C++: An. *J. Appl. Crystallogr.* **2018**, *51* (1), 210–218. https://doi.org/10.1107/S1600576718000183.

(45) Zagorac, D.; Muller, H.; Ruehl, S.; Zagorac, J.; Rehme, S. Recent Developments in the Inorganic Crystal Structure Database: Theoretical Crystal Structure Data and Related Features. *J. Appl. Crystallogr.* **2019**, *52*, 918–925. https://doi.org/10.1107/S160057671900997X.

(46) Scott, H. G. The Estimation of Standard Deviations in Powder Diffraction Rietveld Refinements. *J. Appl. Crystallogr.* **1983**, *16* (2), 159–163. https://doi.org/10.1107/s0021889883010195.

(47) Haywood, B. Y. B. C.; Shinley, R. The Structure of Tetraiodoethylene at 4 K Materials Physics Division , A Tomic Energy Research Establishment , Harwell , Oxfordshire England at Room Temperature Was Reported by Khotsyanova ,. **1977**, 1765–1773.

(48) Berar, J. F.; Lelann, P. E.S.D.'s and Estimated Probable Error Obtained in Rietveld Refinements with Local Correlations. *J. Appl. Crystallogr.* **1991**, *24* (pt 1), 1–5. https://doi.org/10.1107/S0021889890008391.

(49) Nißler, R.; Dennebouy, L.; Gogos, A.; Gerken, L. R. H.; Dommke, M.; Zimmermann, M.; Pais, M. A.; Neuer, A. L.; Matter, M. T.; Kissling, V. M.; de Brot, S.; Lese, I.; Herrmann, I. K. Protein Aggregation on Metal Oxides Governs Catalytic Activity and Cellular Uptake. *Small* **2024**, *2311115*, 1–16. https://doi.org/10.1002/smll.202311115.

(50) Geppert, M.; Hohnholt, M. C.; Thiel, K.; Nürnberger, S.; Grunwald, I.; Rezwan, K.; Dringen, R. Uptake of Dimercaptosuccinate-Coated Magnetic Iron Oxide Nanoparticles by Cultured Brain Astrocytes. *Nanotechnology* **2011**, *22* (14). https://doi.org/10.1088/0957-4484/22/14/145101.

(51) Lin, B.; Zhou, S. Poly(Ethylene Glycol)-Grafted Silica Nanoparticles for Highly Hydrophilic Acrylic-Based Polyurethane Coatings. *Prog. Org. Coatings* **2017**, *106*, 145–154. https://doi.org/10.1016/j.porgcoat.2017.02.008.

(52) Jaqaman, K.; Loerke, D.; Mettlen, M.; Kuwata, H.; Grinstein, S.; Schmid, S. L.; Danuser, G. Robust Single-Particle Tracking in Live-Cell Time-Lapse Sequences. *Nat. Methods* **2008**, *5* (8), 695–702. https://doi.org/10.1038/nmeth.1237.

(53) Stein, S. C.; Thiart, J. TrackNTrace: A Simple and Extendable Open-Source Framework for Developing Single-Molecule Localization and Tracking Algorithms. *Sci. Rep.* **2016**, *6* (July), 1–7. https://doi.org/10.1038/srep37947.